Using tsunami waves reflected at the coast to improve offshore earthquake source parameters: Application to the 2016 Mw 7.1 Te Araroa earthquake, New Zealand

Tatsuya Kubota[1], Tatsuhiko Saito[1], Yoshihiro Ito[2], Yoshihiro Kaneko[3], Laura M. Wallace[3,4], Syuichi Suzuki[5], Ryota Hino[5], and Stuart Henrys[3]

[1]National Research Institute for Earth Science and Disaster Resilience, Tsukuba, Japan.

[2]Disaster Prevention Research Institute, Kyoto Univesity, Uji, Japan.

[3]GNS Science, Lower Hutt, New Zealand.

[4]University of Texas Institute for Geophysics, Austin, Texas, USA.

[5]Graduate School of Science, Tohoku University, Sendai, Japan.

Corresponding author: Tatsuya Kubota (kubotatsu@bosai.go.jp)

Key Points:

- Tsunami from coastal reflected waves associated with the 2016 Te Araroa EQ are clearly observed by offshore ocean bottom pressure gauges
- We greatly reduce uncertainties in the centroid location and fault dimensions of the Te Araroa EQ using tsunami reflected from the coast
- Later tsunami arrivals should be used more widely to extract earthquake source information in the future

Abstract

The Te Araroa earthquake occurred on September 2, 2016 (local time) offshore of the northeastern coast of New Zealand's North Island (Mw 7.1). When this event occurred, ocean bottom pressure gauges (OBPs), installed ~170 km south of the source area, clearly recorded direct tsunami from the source to OBPs (~−1.5 cm), and tsunami from coastal-reflections (~2 cm). We estimate the centroid location that best reproduces the OBP waveforms. When using the direct wave alone, the centroid location is poorly constrained, with a horizontal uncertainty of ~100 km. By combining both direct and reflected tsunami waveforms, we obtain a centroid location near the Global CMT centroid (~80 km northeast from the coast) with smaller uncertainty (~40 km). We also estimate the earthquake source dimension (length and width) and found that the models using coastal reflections require a source dimension larger than ~30 km long. Based on the slip distribution obtained by the finite fault inversion, we obtain an energy-based stress drop $\Delta\sigma_E$ of 1.0 MPa, consistent with typical earthquake stress drop values. This study shows that the information added by coastal reflected tsunami provides much tighter constraints on the centroid location, source dimension, and stress drop of offshore earthquakes, which is difficult to obtain from the onshore seismic data alone. Future studies should utilize the information provided by coastal reflected waves to improve earthquake source modeling using ocean bottom pressure data.

1. Introduction

On 2 September 2016 at 04:37:55 local time (1 September, 16:37:55 UTC), an Mw 7.1 earthquake occurred at 36.98°S, 179.52°E, with a depth of 22 km (http://www.geonet.org.nz/earthquake/2016p661332, Figure 1a). This earthquake was located ~80 km northeast offshore Te Araroa in the Raukumara Peninsula, the North Island, New Zealand (widely referred to as the Te Araroa earthquake). The earthquake had a normal-faulting mechanism and occurred within the subducting Pacific Plate at the Hikurangi subduction zone (Figure 1b) (Warren-Smith et al., 2018). The centroid moment tensor (CMT) solution of the Te Araroa earthquake was estimated using teleseismic data by Global CMT (http://www.globalcmt.org, hereinafter, GCMT) and USGS (http://earthquake.usgs.gov/earthquakes/eventpage/us10006jbi), and from regional seismic data obtained by GeoNet of GNS Science, New Zealand (Ristau, 2008; http://www.geonet.org.nz). Although their depths, strikes, dips, rakes, and seismic moments are similar, their horizontal locations are quite different (Figure 1a, Table 1). Both the GCMT and USGS centroids are located ~80 km northeast from the coast, but they are ~20 km apart from each other in the north-south direction. The GeoNet centroid is located ~50 km northeast from the GCMT and USGS centroids (~130 km from the coast). The Te Araroa earthquake source parameters, and how it fits into the regional tectonic framework is very poorly characterized, due to the earthquake's offshore location and a lack of seismic stations in the offshore region to provide regional azimuthal coverage. Here, we show a new approach that combines modeling of direct tsunami waves with tsunami waves reflected from the coastline to yield greatly improved constraints on the location and source parameters of the Te Araroa earthquake. We suggest that the same approach can be used to improve understanding of other, poorly characterized offshore earthquakes.

It is important to accurately estimate earthquake source parameters to infer earthquake processes, evaluate the physical properties surrounding the rupture area, and to understand how the earthquake plays a role in seismic hazard and the regional geodynamic framework. Many previous studies have assessed the accuracy of the modern worldwide earthquake catalogs, especially CMT catalogs (e.g., Hjörleifsdóttir & Ekström, 2010; Valentine & Trampert, 2012). Seismic waveforms are one of the key pieces of data needed to determine CMT solutions. The seismic waveforms have an advantage of high spatiotemporal resolution, which enables us to extract the source time function, or spatiotemporal evolution of the rupture on the fault plane. In general, the robustness of the estimated source parameters such as centroid location and centroid time is restricted by various factors, such as the azimuthal coverage of seismic stations, S/N ratio, or uncertainties in velocity structure. Although station coverage is improved by teleseismic data, the uncertainty in horizontal centroid locations remains tens of km for global events in many parts of the world that are far from seismic networks (https://earthquake.usgs.gov/earthquakes/eventpage/terms.php). When an earthquake occurs far from the coast, like the Te Araroa earthquake, the azimuthal coverage of regional seismic stations is usually poor and the uncertainty of the centroid horizontal location is large in the direction away from the coast, due to a tradeoff between the centroid time and the horizontal location.

As well as onshore seismic data, tsunami data is often analyzed to constrain earthquake source parameters (e.g., Gusman et al., 2017; Kubota et al., 2015; 2017a), although this approach typically has lower spatiotemporal resolution compared to the seismic waves. On the other hand, because we can use reliable bathymetry data, we can simulate the propagation process of tsunami more accurately than that of seismic waves. Furthermore, because tsunami are not as sensitive to the centroid time difference as seismic wave analyses, the tradeoff between the centroid time and the horizontal location will be much smaller than that of regional seismic data. Tsunami have another advantage in constraining earthquake source dimensions (i.e., fault length and width) as these data contain unique information about the area of seafloor deformation (e.g., the extent of the tsunami source), because the tradeoff between the earthquake source dimension and rupture velocity is much less significant for tsunami than for seismic waves.

When the Te Araroa earthquake occurred, an offshore observation array consisting of four ocean bottom pressure gauges (OBPs) spaced ~ 10 km apart, was located ~ 170 km south of the source area (green triangles in Figure 1a). The long-period signals (period of T ~10 min) were observed by four OBPs, at ~25 min and at ~ 90 min after the mainshock (noted by orange and yellow dots in Figure 1c, respectively). Because there were no other significant earthquakes and aftershocks in this region around the time of the earthquake, these two signals are most likely due to tsunami generated by the Te Araroa earthquake, in spite of the small magnitude (Mw 7.1) and large distance (~ 170 km) of the earthquake from the OBP network. The first tsunami signals are likely to travel directly from the source region (direct tsunami). Because the travel time of the secondary signals at ~90 min is too large compared to the direct tsunami, the secondary signals are probably coastal reflected tsunami waves, which propagate in the shallow water region near the coast and are reflected along the eastern coastline of the Raukumara Peninsula. We should note that such reflected waves are typically excluded from the source estimation analysis and only the direct waves are analyzed because it is often difficult to reproduce the reflected waves in the observed records with numerical simulations.

This study uses tsunami waveforms observed by the offshore OBP array (Figure 1a) to better constrain the centroid location and source dimension of the 2016 Te Araroa earthquake. However, it should be noted that all the available OBPs were located ~ 170 km south of the earthquake location. It is difficult to constrain the centroid location and fault dimensions precisely from the direct waves observed by the OBPs, because the ray paths of the direct waves to the closely-spaced OBP array are similar. To overcome this, we analyze not only the direct tsunami wave arrivals, but also the tsunami waves reflected from the coast. Previous studies have recognized the existence of coastal reflected tsunami waves (e.g., Suppasri et al., 2017; Gusman et al., 2017), but they have not previously been used to constrain the earthquake source parameters. This is likely due to the complexity of the reflected waves, which largely arises from nonlinear effects in shallow water.

2. Ocean Bottom Pressure Data and Data Processing

The OBP array that we use consists of four autonomous instruments equipped with Absolute Pressure Gauges, deployed in early June 2016, and recovered with acoustic release systems mounted on the instruments in late June of 2017. The instruments were located at the stations KU16-2, KU16-3, KU16-4, and KU16-5 (Figure 1a, Table 2). Figure 1c shows the processed pressure records during the time surrounding the Te Araora earthquake. For the processed data, we first removed the ocean-tide components, from the 1-s sampled raw pressure data, using a theoretical tidal model (Matsumoto et al., 2000) (light gray lines in Figure 1c). Then, in order to reduce the high frequency components due to seismic or acoustic waves in the seawater and beneath the seafloor, we took a moving average with a 60-sec time window (dark gray lines), and applied a bandpass filter (Saito, 1978) with a passband of 180 – 3600s (red lines).

Before applying the bandpass filter, the static pressure offset was subtracted using the 20-min average before the focal time.

We recognize large impulsive signals with pressure changes of ~10 hPa with a dominant period T less than ~200 s at the time soon after the focal time (Figure 1c). This is the pressure change caused by seismic waves (e.g., An et al., 2017; Kubota et al., 2017b; Saito, 2013; 2017). There are also coherent tsunami signals between the four OBPs, with maximum amplitude of ~−2 cm at ~25 min from the focal time (orange rectangular area in Figure 2) and another set with ~+1.5 cm at ~90 min (yellow rectangular area). We note that 1 hPa of pressure change is equivalent to 1 cm water height change, assuming a water density of 1.03 g/cm^3. Based on linear long wave theory (e.g., Satake, 1995), the tsunami propagation velocity v is $v = \sqrt{g_0 H}$ where H is the water depth. Assuming the average water depth is 2000 m (e.g., average water depth between the source to the OBPs), we obtain v as ~100 m/s (~6 km/min), and then the travel time becomes ~28 min assuming the epicentral distance is 170 km. This is consistent with the timing of the peak of the first tsunami signals. The duration of the downward wave of the first direct tsunami arrival and the upward wave of the secondary reflected tsunami are ~ 8 – 10 min, which corresponds to a horizontal extent of the subsided area of ~ 48 – 60 km, based on an approximate tsunami propagation velocity around the source region (v ~6 km/min).

3. Tsunami Forward Simulations

In the first step of the analysis, we simulate tsunami records using the CMT solutions estimated by GCMT, GeoNet, and USGS. In this calculation, we assume a rectangular planar fault with uniform slip and calculate the seafloor displacement. The fault length (L) and width (W) are assumed based on fault scaling laws of Wells and Coppersmith (1994) (Table 1). The slip amount on the fault plane (D) is calculated by the following relationship:

$$D = \frac{M_o}{\mu L W}, \tag{1}$$

where M_o is the seismic moment and μ is the rigidity (40GPa). The center of the fault plane (longitude, latitude and depth) is assumed to coincide with the centroid of the CMT solution, since, in the case of a rectangular fault with uniform slip, the centroid is located at the fault center. The strike, dip, and rake angles are fixed to those of each CMT solution. The location and extent of the fault planes are shown by colored rectangles in Figure 2a (red: GCMT, blue: GeoNet, green: USGS). Using these rectangular fault models, permanent seafloor vertical deformation is calculated using the equations of Okada (1992). We adopted the northeast-dipping nodal plane as the fault geometry consistent with double-difference relative hypocenters of the smaller pre-cursory events and the mainshock determined by Warren-Smith et al. (2018).

The region of predicted seafloor deformation for each CMT solution is quite different between the three solutions (Figure 2a). Thus, the tsunami arrival times should also be different between the three CMT solutions. The maximum subsidence expected from the GCMT, GeoNet, and USGS solutions is 18.6 cm, 26.5 cm, and 24.5 cm, respectively. The diameter of the subsided and uplifted areas is ~ 50 km, consistent with the expected source size from the tsunami propagation velocity and the tsunami duration (~ 48 – 60 km).

We then calculate the tsunami by solving the linear long wave (LLW) equation in Cartesian coordinates, using a finite difference scheme on a discretized staggered grid (e.g., Satake, 1995; Saito et al., 2014). We assume that the initial sea surface displacement is equal to the seafloor displacement. As the duration of a typical M~7 earthquake is ~10 – 20 s, which has little effect on the resulting tsunami waves, we assumed instantaneous displacement on the seafloor. We used 250 m resolution gridded bathymetry data from National Institute of Water and Atmospheric Research (NIWA), in New Zealand released in 2016 (https://www.niwa.co.nz/our-science/oceans/bathymetry). The grid spacing used is $\Delta x = \Delta y =$ 500 m, and the time step interval is $\Delta t = 1$ s. To compare the calculated and observed tsunami calculation, we apply a bandpass filter similar to the filter applied to the observed records.

We compare waveforms from the different source models for the station KU16-2 in Figure 2b. The maximum amplitude and duration of the direct waves (~25 min) observed by OBPs are reasonably explained by all CMT solutions. The arrival time matches the GCMT and GeoNet solutions reasonably well, while the match to the USGS solution is worse (orange rectangular area). The GCMT and USGS solutions explain the peak timing of the secondary waves at ~90 min reasonably well, while the GeoNet solution does not (yellow rectangular area). This tendency is also seen in the other OBP waveforms (Figures 2c to 2e). The GCMT solution also matches the tsunami first arrivals observed at the coastal tide gauge at East Cape (Figure 2f), while the GeoNet solution does not. Therefore, we conclude that the GCMT solution's centroid location provides the best match among the three CMT solutions. We also show the comparison of the model results for coastal tide gauges in Figure S1. The calculated waveforms using the GCMT solution do not fit the tide gauges, except for East Cape. This is likely due to the lack of finer grids that accurately capture the bathymetry within bays and ports. This suggests that the use of the offshore OBP data, which is less sensitive to the fine-scale bathymetry, can greatly improve the accuracy of the source parameter estimation of off-shore earthquakes, which is also discussed by Gusman et al. (2017).

We also conduct a tsunami simulation using the finite fault model obtained from teleseismic data, provided by USGS (Figure S2, https://earthquake.usgs.gov/earthquakes/eventpage/us10006jbi#finite-fault). Although the arrival time of the direct and reflected waves is slightly improved compared to that from the rectangular fault based on the USGS solution, the model tsunami wave amplitudes are much smaller than those observed. This suggests that the slip distribution is not well constrained by the teleseismic data. We also simulate the tsunami using the conjugate nodal plane of the GCMT solution (strike of 220°, Figure S3). The calculated seafloor deformation and waveforms are similar to those assuming the northeast-dipping plane (Figure 2), but the amplitudes of the first downward wave are slightly larger than observed (due to the steeper dip and larger normal fault component for the conjugate plane).

In order to test the idea that the secondary tsunami waveform recorded at ~90 min is caused by tsunami reflected from the coast, we conducted an additional tsunami simulation removing the land area (thus the source of reflections does not exist) (Figures 3 and S4). In the calculation, we modified the water depth on the land and near-shore, shallow shelf region ($H <$ 200 m) to equal a constant depth (H = 200m), so that the tsunami does not reflect at the coast (i.e., the coastline does not exist) (Figure 3). We used the GCMT solution to calculate the initial sea surface height, and kept the other settings in the calculation the same as the original ones. The first direct tsunami wave arrival is similar to that obtained using the true bathymetry (Figure 2, compare red and blue lines in Figure 3). However, the secondary tsunami peak at ~ 90 min does not appear in the simulation without the coastline. Even if we assume that the land and the bathymetry shallower than 10 m are modified to a constant sea depth of 10 m, the observed reflected waves cannot be reproduced (red lines in Figure S4), suggesting that the reflection at the coast is required to generate the secondary tsunami waves. Therefore, we conclude that the secondary tsunami represents a coastal reflection from the east coast of the Raukumara Peninsula. Furthermore, the small tsunami wave train prior to the secondary peak (at ~ 60 – 90 min) was not reproduced by the simulation without the land, whereas the simulation that includes bathymetry reproduced this well. This suggests the wave train between 60 – 90 min are also from tsunami reflected at the coast.

To investigate where the strong reflected tsunami signals at ~90 min are radiating from, we conduct some additional analyses (Figures 4, S4 to S8; the details are in Text S1). First, we investigate the snapshots of the tsunami height distribution from the simulations with and without the land (Figures S5a and S5b, respectively), the difference between them (Figure S5c), and their maximum absolute height distribution (Figures S6). We find that the main tsunami energy is directly radiating from the source to the middle part of the East Coast of the Raukumara Peninsula (Figures S6b) and is trapped near the middle section of the East Coast of the Raukumara Peninsula (Figure S6c), indicating that the tsunami largely radiates from the middle part of the East Coast of the Raukumara Peninsula. We also conducted additional tsunami calculations in order to confirm that the coastal reflection occurred in the middle section of the East Coast of the Raukumara Peninsula (Figure S7).~~,~~ We divided the Raukumara Peninsula into three segments (northern, middle, and southern) and we assigned land to each segment but removed the land from the other segments (we modified the water depth shallower than 10 m in the other segments to a constant depth of 10 m) in turn; northern (Figure S7a1), middle (Figure S7a2), or southern (Figure S7a3; see the details in Text S1). The simulation results best reproduce the observed reflected waves at ~90 min when the land is assumed at the middle segment of the Raukumara Peninsula (red lines in Figure S7b2), whereas the simulations that the land is assigned to the other segments (blue: northern, and green: southern) did not (although the tsunami at ~ 70 min are similar to the observation). Therefore we conclude that the coastal reflections are largely radiating from the central part of the eastern coast of the Raukumara Peninsula, and moderately from the northern and southern segments.

We undertake ray tracing of the reflected tsunami using the pseudo-bending method (Um & Thurber, 1987), assuming the reflection points at the middle part of the East Coast of the Raukumara Peninsula and the source at the maximum subsidence of the initial sea surface height calculated based on the GCMT solution (Figure 4). We find that an 85–90-minute travel time of the reflected waves is consistent with the observed data, whereas the travel times are slightly shorter when the source is assumed at the GCMT centroid and at the maximum uplift based on the GCMT solution (Figure S8), indicating the reflected waves at ~ 90 min are mainly generated by the subsidence of tsunami source. We also find that the travel time of the direct tsunami obtained by the ray tracing (dashed line in Figure 4) is approximately 25 min, also consistent with the observations.

We note that the timing of the peak tsunami (Table 2, noted by small dots in Figure 1c) is slightly different between the OBP stations. By using the time delay between the two OBPs, we can estimate the approximate incident azimuth of the direct and reflected tsunamis. We estimate the time delay of tsunami arrivals between the two OBPs, based on cross correlations (Tables S1 and S2, details are described in Text S2). The estimated incident azimuths for the direct and reflected tsunamis are 71° and 29°, respectively (Figure S9). This suggests that the incident azimuth and travel times of the reflected waves are substantially different from those of the direct wave. By using the additional information from the reflected wave, we are able to better constrain the centroid location and the fault dimension.

Accurately modeling tsunami propagation near the coast might require the consideration of nonlinear wave propagation (e.g., Satake, 1995; Saito et al., 2014). In order to assess this, we compared the simulation results derived by the nonlinear long wave (NLL) equation and the LLW equation with the same initial tsunami height distribution and found that the results of the LLW and NLL simulations are almost identical, for both the direct and the reflected waves (Figure S10, details are described in Text S3). We also compare the simulation results using a finer grid spacing ($\Delta x = \Delta y = 250$ m) (Figure S10) and confirm that the difference in the calculated OBP waveforms for grid spacings of 500 m and 250 m are small. However, there are some differences between the two models for the coastal tide gauge (East Cape), particularly for the later arrivals (>~ 60 min). The nonlinearity is small in the OBP waveforms of the Te Araroa earthquake due to the small tsunami amplitude at the coast. If we assume an earthquake with larger magnitude (Mw 8.0) which generates much larger tsunami in the numerical simulation (Figure S11, details are described in Text S3), the nonlinear nature of tsunami would start to appear in the reflected waves.

4. Determination of the Centroid Location

In this section, we determine the earthquake centroid location by reproducing the observed tsunami using a grid search approach, as the horizontal locations of the GCMT, GeoNet, and USGS solutions are somewhat different. We fix the strike, dip, rake, seismic moment, and centroid depth to the GCMT value (GeoNet and USGS values are similar), and we assume the rectangular planar fault dimensions using the GCMT solution discussed earlier (Table 1). Seafloor deformation is calculated using the equations of Okada (1992) and the tsunami is calculated based on the LLW equation (details for tsunami calculation is described in Text S4). We search for the best-fitting horizontal centroid locations in a 300 km × 300 km region, with 5 km intervals. The model waveforms are evaluated based on the variance reduction between the observed and calculated waveforms, VR, expressed as:

$$\mathrm{VR} = \left(1 - \frac{\sum_i^N \left(u_i^{\mathrm{obs}} - u_i^{\mathrm{calc}}\right)^2}{\sum_i^N \left(u_i^{\mathrm{obs}}\right)^2}\right) \times 100\ (\%), \tag{2}$$

where u_i^{obs} and u_i^{calc} are the observed and calculated waveforms, respectively.

At first, we use only the direct waves (time window of 10 – 40 min, orange rectangular area in Figure 5d). An optimum solution is obtained for a centroid located at ~15 km north of the GeoNet centroid (~ 130 km northeast from the coast), shown by a large red star in Figure 5a. The direct waves are reasonably reproduced (VR = 76.3 %), although the reflected waves are not (blue lines in Figure 5d). The centroid locations that gave relatively high VR, are the solutions with a VR of more than 90% of the optimum solution's VR (an area surrounded by green lines in Figure 5a), and extend ~100 km in the WSW-ENE direction. This suggests the centroid location is not well-constrained by the direct wave alone.

To evaluate why the high-VR area spans a larger region aligned in the WSW-ENE direction, we conduct ray-tracing of tsunami from the OBPs to the solutions with high VR (Figure S12). Most of the rays from solutions with high VR arrive at the OBPs with similar travel times of 22–24 min. Moreover, the incident azimuth to the OBPs from the solutions in the high-VR area are similar (~60 – 65°). These make it difficult to resolve the differences in the centroid horizontal location. We note that the incident azimuths are consistent with that expected from the time delay of the tsunami arrival at the OBP array.

We also use tsunami reflected from the coast (70 – 100 min) in addition to the direct tsunami (10 – 40 min) to estimate the centroid location (Figure 5b). We obtain a centroid location at ~10 km northwest of the GCMT centroid (178.97°E, 37.10°S, ~ 80 km northeast from the coast), which is part of the high-VR area estimated by the direct wave alone (Figure 5a). The extent of the high-VR area is reduced to ~40 km in the WSW–ENE direction and does not coincide with the GeoNet and USGS centroids. The calculated reflected waves reasonably reproduced the observed, as well as the direct waves (red lines in Figure 5d, VR = 73.2 %). Note that the optimum solution estimated from the direct wave alone (Figure 5a) did not explain the amplitudes and the arrival times of the reflected waves, as well as the forward-calculated waveforms from the GeoNet solution. When we used the reflected wave alone, we observe a similar tendency (Figure 5c). The centroid was located at 178.92°E, 37.15°S, 5 km west and 5 km south of that from both direct and reflected waves. The incident azimuth and travel times of the reflected waves are substantially different from the direct waves (Figure S9). Using the additional information from the reflected waves, we can reduce the uncertainty in the centroid location.

5. Estimation of the Fault Dimension

We then undertake a search for the earthquake source dimensions (Figure 6). We fix the #2
centroid depth of the rectangular fault to the GCMT centroid (27.8 km), the seismic moment M_o and fault strike, dip, and rake to the GCMT value, and we fix the centroid location (longitude and latitude) to that obtained from the grid search of the centroid location using both the direct and reflected waves (Figure 5b). We assume the ratio of source length L to width W such that L/W = 2, with a rigidity of μ = 40 GPa (note that the source dimension ratio expected from the GCMT solution and the scaling law of Wells & Coppersmith (1994) is ~2; L = 45.1 km and W = 21.6 km, Table 1), and vary the fault length L at 5 km intervals. We show the result using only the direct waves in Figure 6 (blue curve). Considering the range of solutions with VRs larger than 90 % of the optimum solution, we estimate the source length uncertainty as L = 40 km ± 20 km. When

using both the direct and reflected waves, we find that the optimum source length is L = 50 ± 10 km (red curve in Figure 6). In both analyses, the upper limit of the possible source length is similar (~60 km). However, the results using both the direct and reflected waves suggest that a smaller source dimension (L < 30 km) is not plausible. Moreover, source dimensions of L < 40 km also seem improbable when using the reflected waves alone (green curve in Figure 6).

To evaluate how sensitive the calculated waveforms are to source dimension, we compare the calculated waveforms at the station KU16-2 for a variety of source dimensions (Figure 7) (see Figure S13 for other stations). The tsunami with larger fault dimensions (L > ~ 60 km) have smaller amplitude and longer duration for the direct waves, compared to the observations. When the fault dimensions are small (e.g., L < ~ 40 km), the amplitudes of the model reflected waves are larger compared to the observations, especially for the earlier part of the reflected wave (70 – 85 min). Fault dimensions with L ~40 – 60 km provide a reasonable fit to the observed tsunami waveform amplitude and duration.

By using the coastal reflected tsunami waveforms, we obtain better constraints on the source dimension. Our source dimension estimated from the scaling rules of Wells and Coppersmith (1994) (Table 1) is similar to the solution obtained from both direct and reflected waves. In contrast, Warren-Smith et al. (2018) suggested the possibility that the source dimension is larger than expected from typical fault scaling relationships, based on investigation of the GeoNet seismograms (see Section 4.2 in Warren-Smith et al. (2018)). Using the range of source dimensions obtained from the analysis of both the direct and reflected waves, we calculate the stress drop $\Delta\sigma$, based on the conventional relationship of Kanamori and Anderson (1975), as:

$$\Delta\sigma = c\frac{\mu D}{\sqrt{LW}} \qquad (3)$$

where c is constant. Assuming Poisson's ratio of 0.25, we obtain c = $8/3\pi$. Assuming $L = 2W$ and using the seismic moment, we rewrite equation (3) as,

$$\Delta\sigma = c\frac{2\sqrt{2}M_o}{L^3}. \tag{4}$$

Substituting the estimated values of L = 40 – 60 km, we obtain a possible range of stress drops $\Delta\sigma$ = 0.5 – 3.0 MPa. This value is consistent with typical values for earthquake stress drops (~ 1 – 10 MPa) (e.g., Abe, 1975; Kanamori & Anderson, 1975).

6. Finite Fault Inversion

In order to investigate the stress drop in more detail, we conduct a finite fault inversion to estimate the slip distribution (e.g., Satake, 1989), using the direct and reflected tsunami waves. The details of the inversion are shown in Text S5. We assume a rectangular planar fault 80 km long and 70 km wide, based on the optimum fault dimension obtained by the grid search. The center of the assumed fault coincides with the optimum centroid obtained by the grid search (Figure 5b). We use the fault geometry (strike, dip, and rake) from the GCMT solution. We divided the planar fault into the subfaults with size-5 km × 5 km, and use these to calculate the Green's functions for the inversion. In the inversion, we impose a non-negativity constraint (Lawson & Hanson, 1978) and a spatial smoothing constraint. The weighting of the smoothing is based on the value of Akaike's Bayesian Information Criterion (ABIC) (Yabuki & Matsu'ura, 1992) (Figure S14).

We show the inversion result using both direct and reflected waves in Figure 8 (the results using the direct waves alone and using the reflected waves alone are shown in Figure S15). The centroid of slip calculated from the finite fault model (white star in Figure 8) is located near the center of the assumed fault plane, which coincides with the centroid obtained by the grid search.

We obtain a maximum slip of 0.9 m, and the total seismic moment M_o is 4.34 $\times 10^{19}$ Nm (Mw 7.03, assuming μ = 40 GPa). The main rupture area, defined as the subfaults with slip larger than 20 % of the maximum slip (86 % of the total moment is concentrated in this area, marked by green lines in Figure 8), has an area of 2000 km^2 and the average slip amount within the main rupture area is ~ 0.5 m. We calculate the shear stress distribution (Figure S16) from the finite fault model, to estimate an energy-based stress drop ($\Delta\sigma_E$) (Noda et al., 2013; Ye et al., 2016) (the details are described in Text S5). We obtain $\Delta\sigma_E$ of 1.0 MPa, which is included within the uncertainty range obtained by the grid search ($\Delta\sigma$ ~ 0.5 – 3.0 MPa), but is at the lower end of typical earthquake stress drop values (~ 1 – 10 MPa) (e.g., Abe, 1975; Kanamori & Anderson, 1975; Ye et al., 2016). The low stress drop of our estimation is consistent with Warren-Smith et al. (2018), who suggested that the source dimension is larger than expected from typical fault scaling relationships. However, we note that the estimated stress drop is larger than stress drops observed in tsunami earthquakes (Kanamori, 1972; Tanioka & Satake, 1996), which are characterized by extremely low stress drops (< ~ 0.5 MPa) (e.g., Ye et al., 2016). This is expected given the intra-slab source of the Te Araora earthquake (tsunami earthquakes are typically generated on the shallow plate interface, not within the slab).

7. Discussion and Conclusions

Ocean bottom pressure gauges (OBPs) deployed in the offshore region clearly showed small tsunamis associated with the 2016 Te Araroa earthquake (Mw 7.1). In addition to the direct-arrival tsunami with ~−1.5 – 2 cm height, tsunami waveforms with ~ +2 cm height reflected from the coast were recorded ~60 min after the direct tsunami arrival. By analyzing the reflected tsunamis in addition to the direct tsunami, we improved estimates of the centroid location and fault dimensions of the 2016 Te Araroa earthquake. Although the centroid locations of the GCMT and GeoNet CMT solutions are quite different (~ 80 km apart from each other), both the tsunami forward models provided a reasonable fit to the observed direct wave. However, we found that the GCMT solution reproduced the reflected waves well, while the GeoNet solution did not. When we used both direct and reflected waves, the horizontal extent of the possible centroid location was constrained to within ~40 km (compared to ~100 km for the direct wave solution). We also undertook a grid search on the source dimensions (source length and width). Using only direct waves, we obtained an optimum source dimension of L = 40 km ± 20 km. However, by including reflected waves in the estimate of the source dimension, the source dimension was estimated as L = 50 ± 10 km, which suggests that a source dimension < 40 km long is unlikely. Our finite fault inversions suggest that the main slip was concentrated at the location of the fault obtained by the grid search for the horizontal fault location. Using the finite fault model, we obtained an energy-based stress drop for this earthquake of 1.0 MPa. This value is in the range of typical earthquake stress drops, albeit on the low end of these.

Combining direct and coastal reflected waves observed by offshore OBPs, we can estimate the centroid horizontal location, fault dimensions, and stress drop of the Te Araroa earthquake more accurately than using direct tsunami wave arrivals and onshore seismic station data alone. The effect of nonlinearity in the OBP waveforms is very small in moderate (M ~ 7) earthquakes because of the small tsunami amplitude at the coast. Coastal reflected tsunami waves have not been used previously for estimating earthquake source parameters, although the characteristics of coastal reflected waves have been noted by some previous studies (Saito et al., 2013; 2014; Gusman et al., 2017; Suppasri et al., 2017). Coastal reflected tsunamis waveforms are very useful to improve source parameter estimation, especially for moderate size offshore earthquakes

(M < ~ 7), which are often difficult to constrain because of the small amplitude of the signal at onshore seismic stations.

Since dense and wide seafloor tsunami observation networks have been constructed in the deep ocean (e.g., Kaneda et al., 2015; Kawaguchi et al., 2015; Kanazawa et al., 2016; Uehira et al., 2016), it is anticipated that later tsunami arrivals including coastal reflected tsunami signals will be recorded more often from these OBP arrays. In the past, when the details of the bathymetry were not well-known in many locations, reflected waves could not be simulated reliably. For example, Figure S17 demonstrates how low-resolution bathymetry data cannot reproduce the reflected tsunami. We calculate tsunami using the ETOPO1 global bathymetry data, with a spatial resolution of 1 arcmin (~ 1.5 km) (Amante & Eakins, 2009) (we use the LLW equation with a grid spacing of $\Delta x = \Delta y = 2$ km and an initial sea surface height distribution obtained from the finite fault inversion; Figure 8). The direct tsunami waves (~ 10 – 40 min) agree well with the observed waveforms even with the low-resolution bathymetry data, while the reflected tsunami waves (~ 70 – 100 min) do not match the observations, demonstrating the dependence of reflected waves on the details of the bathymetry. Tsunami simulations including high-resolution bathymetry data, enable us to simulate the reflected tsunami more reliably than the past. This is similar to the advances made in seismology that utilize reflected waves and scattered seismic waves (coda waves) to improve understanding of the earthquake source (e.g., Aki, 1969; Umino et al., 1995; Engdahl et al., 1998; Abercrombie, 2013). The analysis of later tsunami arrivals holds great promise as a new tool to advance future tsunami research.

Acknowledgments, Samples, and Data

We thank Editor Yehuda Ben-Zion and two anonymous reviewers for their constructive comments. This study was supported by JSPS KAKENHI 26257206 and partially supported by JP26000002. We greatly appreciate the contribution by the captain and crew of the *R/V Tangaroa* during, TAN1607, and the ocean bottom observation engineering teams from Kyoto University and Tohoku University to obtain the OBP data. We downloaded GeoNet tide gauge data, via IOC (Intergovernmental Oceanographic Commission)'s Sea Level Station Monitoring Facility (http://www.ioc-sealevelmonitoring.org/).We acknowledge support for ship time from New Zealand’s Ministry of Business Innovation and Employment (MBIE), and support from MBIE’s Endeavour fund program. The figures in this paper were prepared using Generic Mapping Tools (GMT) (Wessel & Smith, 1998). The OBP data used in this study is available in the supplementary file (Supplementary Dataset S1).

References

Abercrombie, R. E. (2013). Comparison of direct and coda wave stress drop measurements for the Wells, Nevada, earthquake sequence. *Journal of Geophysical Research: Solid Earth*, 118, 1458–1470. http://doi.org/10.1029/2012JB009638.

Aki, K. (1969). Analysis of the seismic coda of local earthquakes as scatted waves. *Journal of Geophysical Research*, 74, 615–631. http://doi.org/10.1029/JB074i002p00615

Amante, C., & Eakins, B. W. (2009). ETOPO1 1 arc-minute global relief model: Procedures, data sources and analysis. In *NOAA Technical Memorandum NESDIS NGDC-24*. Boulder, CO: National Geophysical Data Center, NOAA. http://doi.org/10.7289/V5C8276M

Abe, K. (1975). Reliable estimation of the seismic moment of large earthquakes. *Journal of Physics of the Earth*, *23*, 381–390. http://doi.org/10.4294/jpe1952.23.381

An, C., Cai, C., Zheng, Y., Meng, L., & Liu, P. (2017). Theoretical Solution and Applications of Ocean Bottom Pressure Induced by Seismic Seafloor Motion. *Geophysical Research Letters*, *44*, 10272–10281. http://doi.org/10.1002/2017GL075137

Engdahl, E.R., van der Hilst, R., & Buland, R. (1998). Global teleseismic earthquake relocation with improved travel times and procedures for depth determination. *Bullutin of Seismologcal Society of America*, 88, 722–743.

Gusman, A. R., Satake, K., Shinohara, M., Sakai, S., & Tanioka, Y. (2017). Fault Slip Distribution of the 2016 Fukushima Earthquake Estimated from Tsunami Waveforms. *Pure and Applied Geophysics*, *174*, 2925–2943. http://doi.org/10.1007/s00024-017-1590-2

Hjörleifsdóttir, V., & Ekström, G. (2010). Effects of three-dimensional Earth structure on CMT earthquake parameters. *Physics of the Earth and Planetary Interiors*, *179*, 178–190. http://doi.org/10.1016/j.pepi.2009.11.003

Kanamori, H. (1972). Mechanism of tsunami earthquakes. *Physics of the Earth and Planetary Interiors*, *6*, 346–359. http://doi.org/10.1016/0031-9201(72)90058-1

Kanamori, H., & Anderson, D. L. (1975). Theoretical basis of some empirical relations in seismology. *Bulletin of the Seismological Society of America*, *65*(5), 1073–1095.

Kanazawa, T., Uehira, K., Mochizuki, M., Shinbo, T., Fujimoto, H., Noguchi, S. … Okada, Y. (2016). *S-net project, cabled observation network for earthquakes and tsunamis*, WE2B–3, Paper presented at SubOptic 2016, SubOptic, Dubai.

Kaneda, Y., Kawaguchi, K., Araki, E., Matsumoto, H., Nakamura, T., Kamiya, S … Takahashi, N. (2015). Development and application of an advanced ocean floor network system for megathrust earthquakes and tsunamis. In Favali P. et al. (Eds.), *Seafloor Observatories* (pp. 643–662). Berlin: Springer

Kawaguchi, K., Kaneko, S., Nishida, T. & Komine, T. (2015). Construction of the DONET real-time seafloor observatory for earthquakes and tsunami monitoring. In Favali P. et al. (Eds.), *Seafloor Observatories* (pp. 211–228). Berlin: Springer.

Kubota, T., Hino, R., Inazu, D., Ito, Y., & Iinuma, T. (2015). Complicated rupture process of the Mw 7.0 intraslab strike-slip earthquake in the Tohoku region on 10 July 2011 revealed by near-field pressure records. *Geophysical Research Letters*, *42*, 9733–9739. http://doi.org/10.1002/2015GL066101

Kubota, T., Hino, R., Inazu, D., Ito, Y., Iinuma, T., Ohta, Y., … Suzuki, K. (2017a). Coseismic slip model of offshore moderate interplate earthquakes on March 9, 2011 in Tohoku using tsunami waveforms. *Earth and Planetary Science Letters*, *458*, 241–251. http://doi.org/10.1016/j.epsl.2016.10.047

Kubota, T., Saito, T., Suzuki, W., & Hino, R. (2017b). Estimation of Seismic Centroid Moment Tensor Using Ocean Bottom Pressure Gauges as Seismometers. *Geophysical Research Letters*, *44*, 10907–10915. http://doi.org/10.1002/2017GL075386

Lawson, C. L. & Hanson, B.J. (1974). *Solving Least Squares Problems*. Philadelphia, PA: Society for Industrial and Applied Mathematics. http://doi.org/10.1137/1.9781611971217

Matsumoto, K., Takanezawa, T., & Ooe, M. (2000). Ocean tide models developed by assimilating TOPEX/POSEIDON altimeter data into hydrodynamical model: A global model and a regional model around Japan. *Journal of Oceanography*, *56*, 567–581. http://doi.org/10.1023/A:1011157212596

Noda, H., Lapusta, N., & Kanamori, H. (2013). Comparison of average stress drop measures for ruptures with heterogeneous stress change and implication for earthquake physics. *Geophysical Journal International*, 193, 1691–1712. http://doi.org/10.1093/gji/ggt074

Okada, Y. (1992). Internal deformation due to shear and tensile faults in a half-space. *Bulletin of the Seismological Society of America*, *82*(2), 1018–1040.

Ristau, J. (2008). Implementation of routine regional moment tensor analysis in New Zealand. *Seismological Research Letters*, *79*(3), 400–415. http://doi.org/10.1785/gssrl.79.3.400

Saito, M. (1978). An automatic design algorithm for band selective recursive digital filters. *Butsuri Tanko*, 31, 112–135. (in Japanese).

Saito, T. (2013). Dynamic Tsunami generation due to sea-bottom deformation: Analytical representation based on linear potential theory. *Earth, Planets and Space*, *65*, 1411–1423. http://doi.org/10.5047/eps.2013.07.004

Saito, T. (2017). Tsunami Generation: Validity and Limitations of Conventional Theories. *Geophysical Journal International*, *210*, 1888–1900. http://doi.org/10.1093/gji/ggx275

Saito, T., Inazu, D., Tanaka, S., & Miyoshi, T. (2013). Tsunami coda across the Pacific Ocean following the 2011 Tohoku-Oki earthquake. *Bulletin of the Seismological Society of America*. 103(2B), 1429–1443. http://doi.org/10.1785/0120120183

Saito, T., Inazu, D., Miyoshi, T., & Hino, R. (2014). Dispersion and nonlinear effects in the 2011 Tohoku-Oki earthquake tsunami. *Journal of Geophysical Research: Oceans*, *119*, 5160–5180. http://doi.org/10.1002/2014JC009971

Satake, K. (1989). Inversion of tsunami waveforms for the estimation of heterogeneous fault motion of large submarine earthquakes: The 1968 Tokachi-oki and 1983 Japan Sea earthquakes. *Journal of Geophysical Research*. 94(B5), 5627–5636. http://doi.org/10.1029/JB094iB05p05627

Satake, K. (1995). Linear and nonlinear computations of the 1992 Nicaragua earthquake tsunami. *Pure and Applied Geophysics*, *144*, 455–470. http://doi.org/10.1007/BF00874378

Suppasri, A., Leelawat, N., Latcharote, P., Roeber, V., Yamashita, K., Hayashi, A., … Imamura, F. (2017). The 2016 Fukushima earthquake and tsunami: Local tsunami behavior and recommendations for tsunami disaster risk reduction. *International Journal of Disaster Risk Reduction*, *21*, 323–330. http://doi.org/10.1016/j.ijdrr.2016.12.016

Tanioka, Y., & Satake, K. (1996). Fault parameters of the 1896 Sanriku tsunami earthquake estimated from tsunami numerical modeling. *Geophysical Research Letters*, *23*(13), 1549–1552. http://doi.org/10.1029/96GL01479

Uehira, K., Kanazawa, T., Mochizuki, M., Fujimoto, H., Noguchi, S., Shinbo, T. … Yamada, T. (2016). *Outline of Seafloor Observation Network for Earthquakes and Tsunamis along the Japan Trench (S-net)*, EGU2016-13832, Paper presented at EGU General Assembly 2016, European Geosciences Union, Vienna, Austria.

Um, J., & Thurber, C. (1987). A fast algorithm for two-point seismic ray tracing. *Bulletin of the Seismological Society of America*, *77*, 972–986.

Umino, N., Hasegawa, A., & Matsuzawa T. (1995). *sP* depth phase at small epicentral distances and estimated subducting plate boundary. *Geophysical Journal International*, 120, 356–366. doi:10.1111/j.1365-246X.1995.tb01824.x

Valentine, A. P., & Trampert, J. (2012). Assessing the uncertainties on seismic source parameters: Towards realistic error estimates for centroid-moment-tensor determinations. *Physics of the Earth and Planetary Interiors*, *210–211*, 36–49. http://doi.org/10.1016/j.pepi.2012.08.003

Warren-Smith, E., Fry, B., Kaneko, Y., & Chamberlain, C. J. (2018). Foreshocks and delayed triggering of the 2016 M_W7.1 Te Araroa earthquake and dynamic reinvigoration of its aftershock sequence by the M_W7.8 Kaikōura earthquake, New Zealand. *Earth and Planetary Science Letters*, *482*, 265–276. http://doi.org/10.1016/j.epsl.2017.11.020

Wells, D. L., & Coppersmith, K. J. (1994). New Empirical Relationships among Magnitude, Rupture Length, Rupture Width, Rupture Area, and Surface Displacement. *Bulletin of the Seismological Society of America*, *84*(4), 974–1002.

Wessel, P., & Smith, W. H. F. (1998). New, improved version of generic mapping tools released. *Eos, Transactions American Geophysical Union*, *79*, 579. http://doi.org/10.1029/98EO00426

Williams, C. A., Eberhart-Phillips, D., Bannister, S., Barker, D. H. N., Henrys, S., Reyners, M., & Sutherland, R. (2013). Revised Interface Geometry for the Hikurangi Subduction Zone, New Zealand. *Seismological Research Letters*, *84*(6), 1066–1073. http://doi.org/10.1785/0220130035

Yabuki, T., & Matsu'ura M. (1992). Geodetic data inversion using a Bayesian information criterion for spatial distribution of fault slip. *Geophysical Journal International*, 109, 363–375. http://doi.org/10.1111/j.1365-246X.1992.tb00102.x

Ye, L., Lay, T., Kanamori, H., & Rivera, L. (2016). Rupture characteristics of major and great ($M_w \geq$ 7.0) megathrust earthquakes from 1990 to 2015: 1. Source parameter scaling relationships. *Journal of Geophysical Research: Solid Earth*, *121*(2), 826–844. http://doi.org/10.1002/2015JB012426

Table 1. CMT parameters and fault parameters used for forward calculation

Parameter	Global CMT	GeoNet	USGS
Origin time (hh:mm:ss UTC)	16:38:15.8[d]	16:37:55.440	16:37:57.3
Longitude [°E]	179.03	179.5200	179.06
Latitude [°S]	37.19	36.9795	37.26
Depth [km]	27.8	23	25.5
Seismic moment M_o [Nm]	5.05×10^{19}	6.35×10^{19}	4.410×10^{19}
Mw	7.1	7.1	7.0
Strike [°][a]	354 / 220	354 / 224	351 / 229
Dip [°][a]	20 / 70	21 / 76	26 / 75
Rake [°][a]	−134 / −76	−138 / −74	−145 / −68
Length L [km][b]	45.13	48.71	43.13
Width W [km][b]	21.58	22.77	20.91
Slip amount D [m][c]	1.30	1.43	1.22

[a] Parameters for two conjugate nodal planes are shown. We used the east-dipping nodal plane (strike ~ 354°) for the calculation.

[b] Length (L) and width (W) were assumed based on the scaling law of Wells and Coppersmith (1994).

[c] Slip amount (D) is calculated from $D = M_o/(\mu LW)$, assuming μ = 40 GPa.

[d] Note that the centroid time is shown.

Table 2. Locations of the OBP stations and peak timing of tsunamis.

Station	Longitude [°E]	Latitude [°S]	Depth [m]	Peak timing [min][a]	
				Direct wave	Reflected wave
KU16-2	178.8729	38.8465	2,138	25.4	93.6
KU16-3	178.7555	38.8914	1,379	27.0	93.6
KU16-4	178.6609	38.7112	1,047	26.8	91.8
KU16-5	178.8950	38.7208	2,450	24.6	91.9

[a] Peak time is measured from the focal time. These are noted by small dots in Figure 1c.

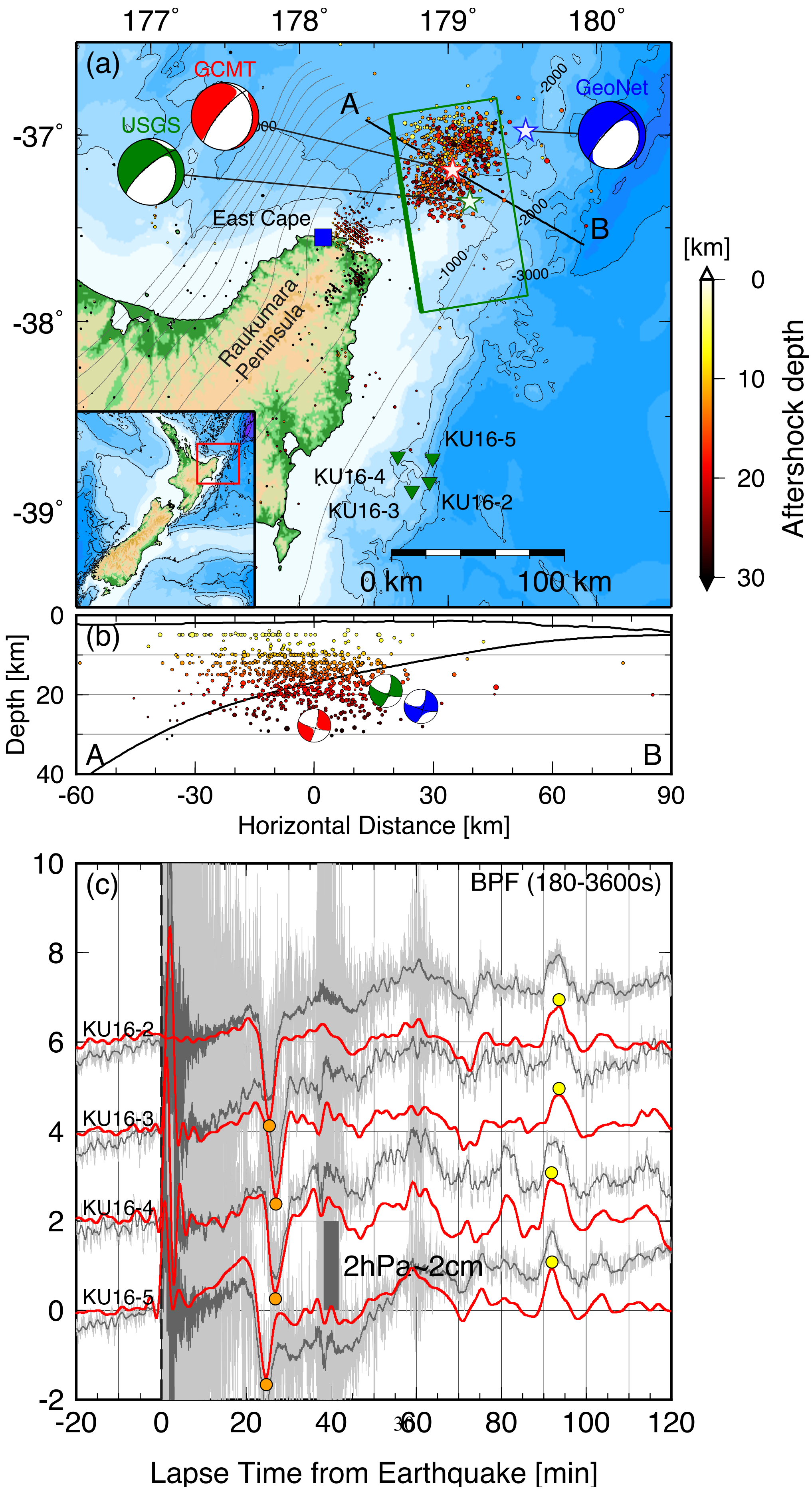

177°
178°
179°
180°
-37°
-38°
-39°
(a)
GCMT
USGS
GeoNet
A
B
East Cape
Raukumara Peninsula
KU16-5
KU16-4
KU16-3
KU16-2
0 km
100 km
[km]
0
10
20
30
Aftershock depth
(b)
Depth [km]
Horizontal Distance [km]
(c)
BPF (180-3600s)
2hPa~2cm
Lapse Time from Earthquake [min]

589

Figure 1. (a) Location map of this study. The green inverted triangles denote the OBP stations used for the analysis. The blue square is the location of the coastal tide gauge at East Cape. The CMT solutions and the centroid locations from GCMT (red), GeoNet (blue), and USGS (green) are shown. The green rectangle denotes the location of the finite fault model provided by USGS. The contour lines of the bathymetry are drawn at 1000 m intervals. Small circles denote the aftershock distribution determined by GeoNet, until 14 September 2016. Thin gray contour lines show the subducting plate interface from Williams et al. (2013), with 10 km depth intervals. (b) Vertical cross section along the A-B line in Figure 1a. The thick black curve is the Hikurangi plate interface from the model of Williams et al. (2013). (c) Pressure time series observed at the OBPs. Light and dark gray waveforms denote the raw and moving-averaged pressure time series, respectively. Red waveforms are obtained by applying a bandpass filter to the moving-averaged data. In the application of the bandpass filter, we set the parameters of Saito (1978) as A_p=0.50, A_s=5.00, F_s = 1/120 Hz, F_p = 1/180 Hz, and F_l=1/3600 Hz. Small filled dots denote the peak timing of the direct (orange) and reflected tsunamis waveform arrivals (yellow).

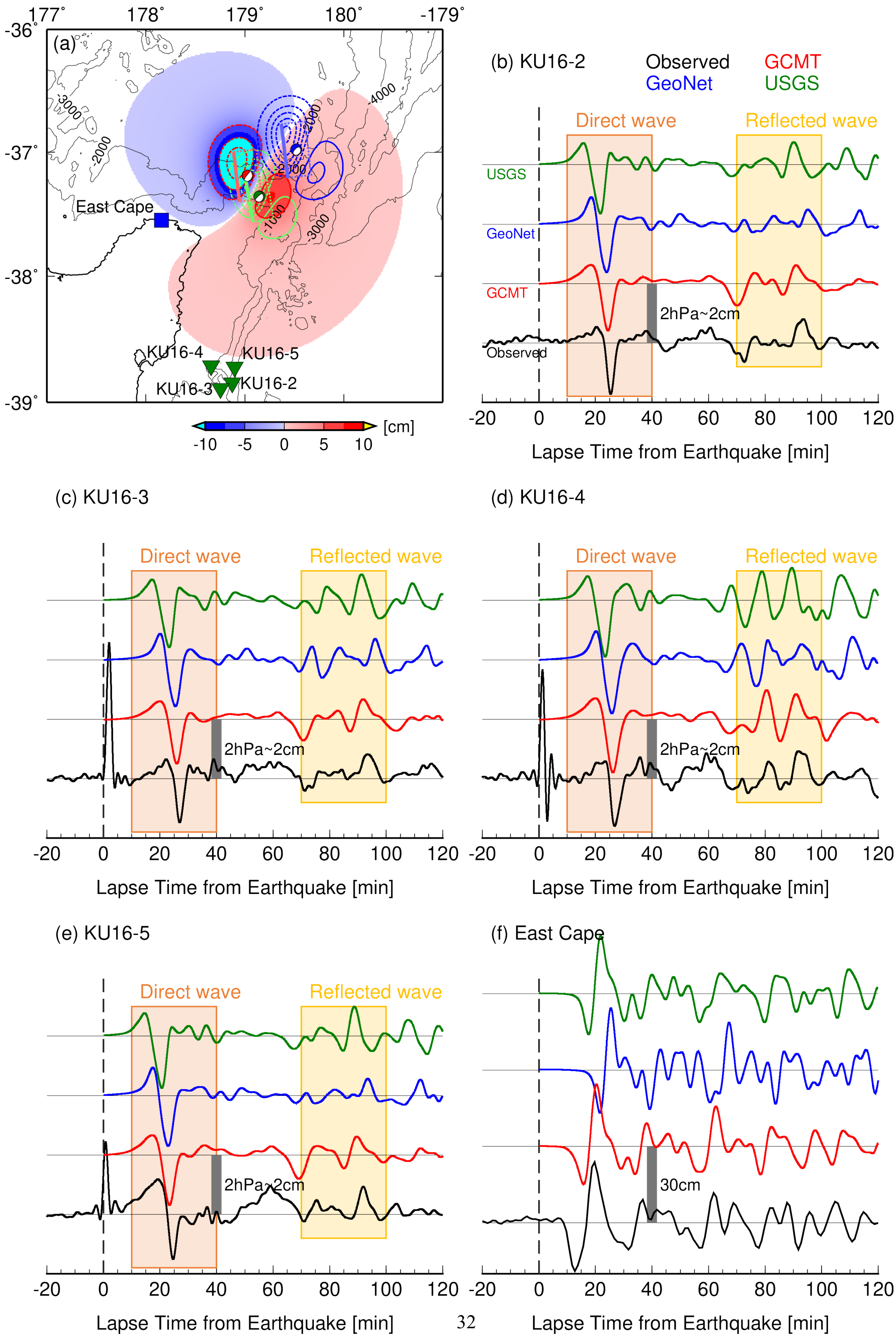
(a)
177˚
178˚
179˚
180˚
-179˚
-36˚
-37˚
-38˚
-39˚
East Cape
KU16-4
KU16-5
KU16-3
KU16-2
-3000
-2000
-4000
-1000
[cm]
-10
-5
0
5
10
(b) KU16-2
Observed
GeoNet
GCMT
USGS
Direct wave
Reflected wave
2hPa~2cm
(c) KU16-3
(d) KU16-4
(e) KU16-5
(f) East Cape
30cm
Lapse Time from Earthquake [min]
-20
0
20
40
60
80
100
120

604

Figure 2. (a) Initial tsunami height distributions calculated from the CMT solutions. Background colors (red and blue) show the initial tsunami height distribution calculated from the GCMT solution. Colored rectangles and contour lines denote the fault models and tsunami source distribution, calculated from the GCMT (red), GeoNet (blue), and USGS (green) solutions (contour intervals are 5 cm). Comparison of the forward-calculated waveforms based on the CMT solutions, where trace colors match the corresponding fault models used in (a), at the stations (b) KU16-2, (c) KU16-3, (d) KU16-4, (e) KU16-5, and (f) East Cape.

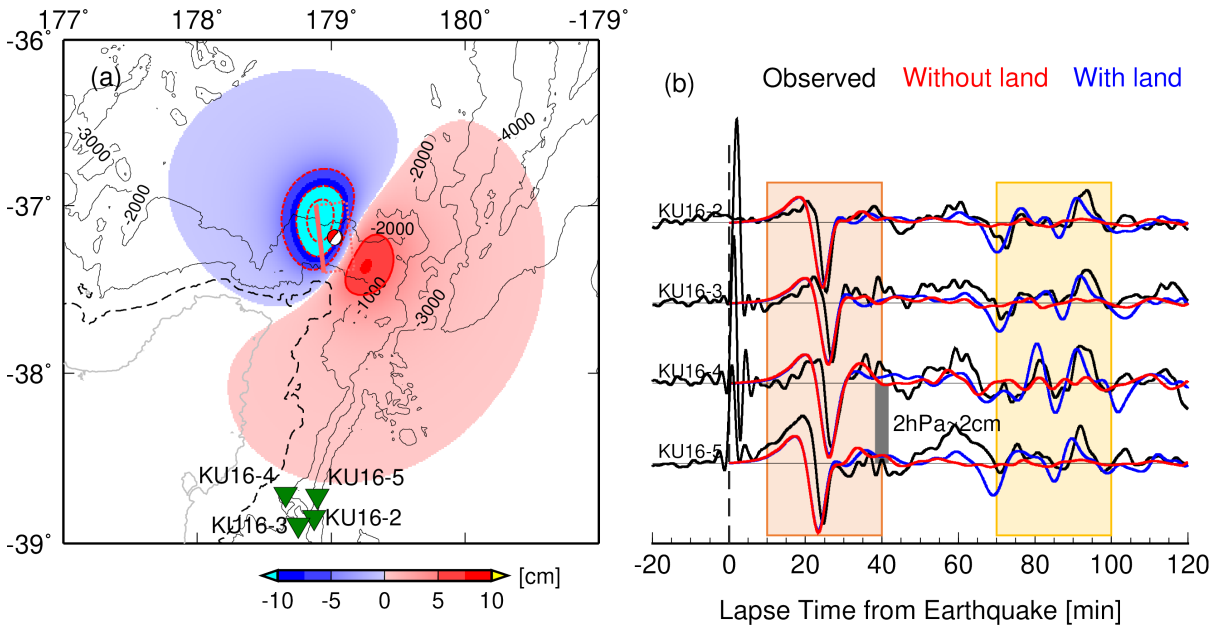

Figure 3. Comparison of the observed (black) and calculated waveforms based on the GCMT solutions, with (blue) and without (red) the land. In the calculation that excludes land, we modified the water depth in the shallow region (H < 200 m) to a constant depth (H =200 m). The 200 m iso-depth contour from the true bathymetry is noted by the dashed line.

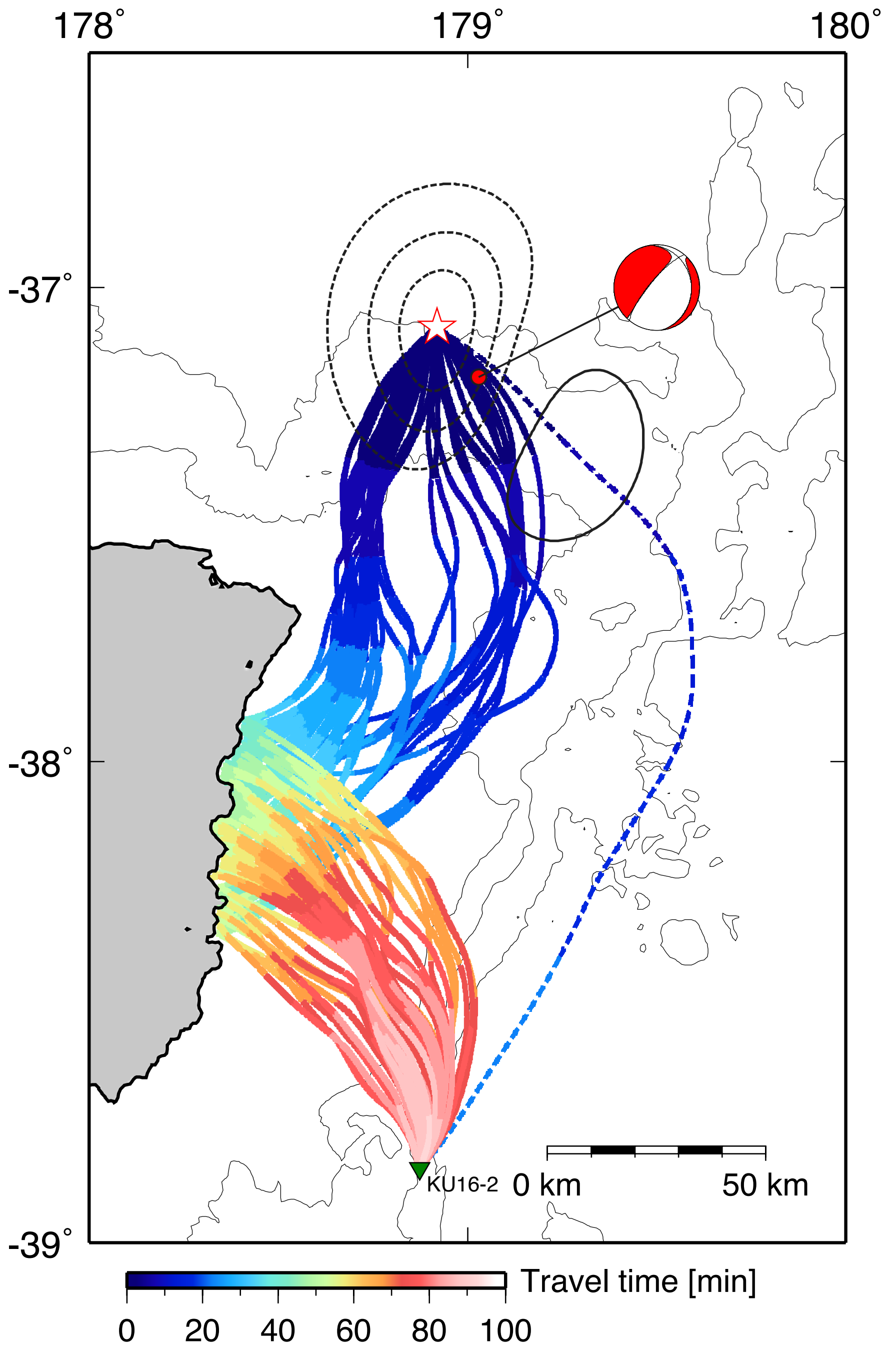

617 **e**

618 **Figure 4.** Ray tracing of the coastal reflected tsunami waves, assuming a source at the maximum
619 subsidence expected from the GCMT solution. Red star denotes the location of the assumed
620 source. The dashed lines denote the ray paths of the direct tsunami waves. Colors of the rays of
621 the reflected tsunami waves denote the travel time.

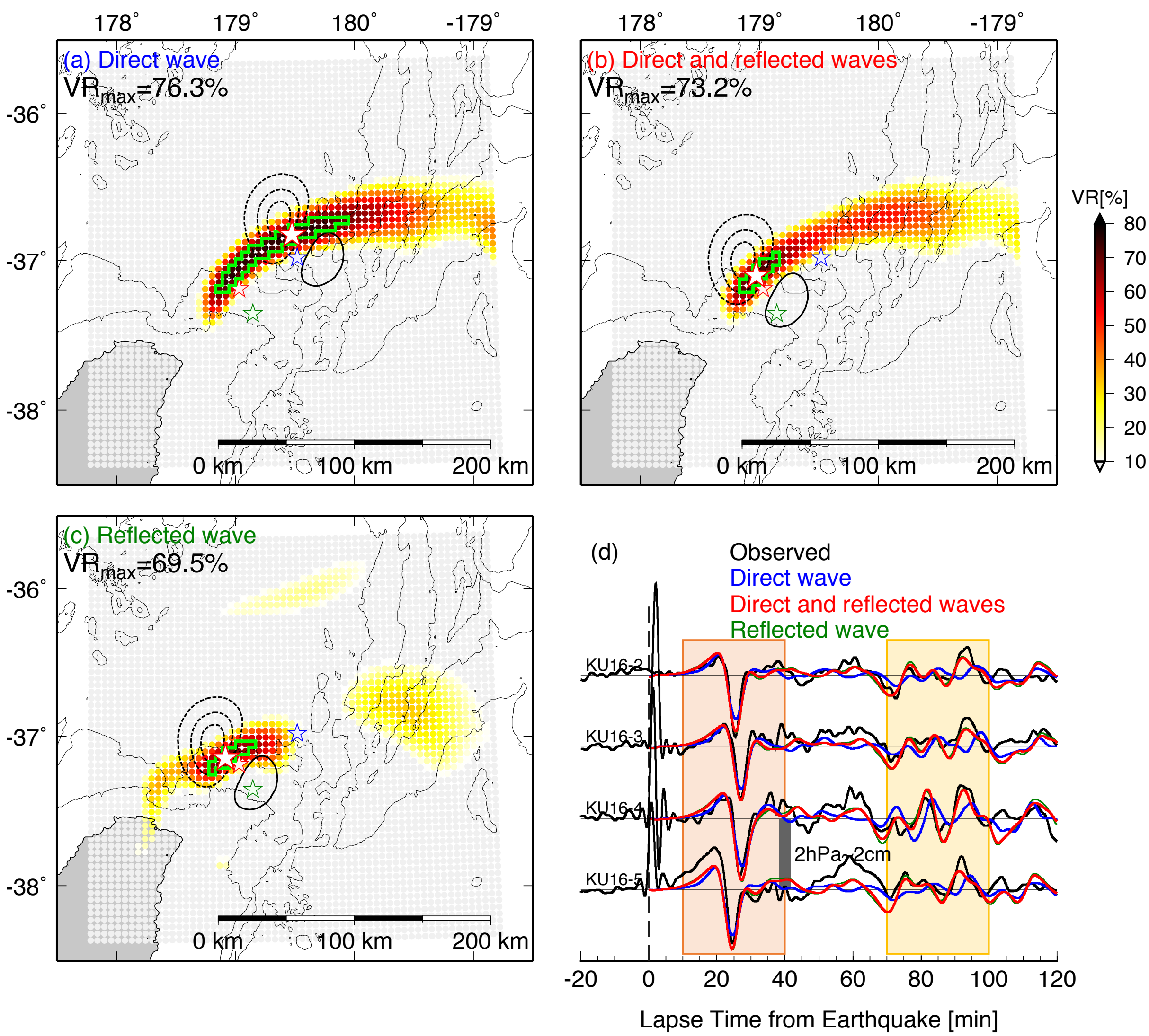

Figure 5. Results of the grid search for the centroid location, using (a) only the direct waves, (b) both direct and reflected waves, and (c) only the reflected waves. (a–c) Distribution of the VR between the calculated and observed waveforms. The large red star denotes the location of the optimum centroid location. The areas surrounded by the green contour are the solutions with relatively high VR (> 90 % of the optimum VR). Locations of the CMT centroids are also shown by small stars (GCMT: red, GeoNet: blue, USGS: green). (d) Comparison of the waveforms

between the observed (black) and calculated waveforms from direct waves alone (blue), both direct and reflected waves (red), and reflected waves alone (green), for each OBP station. The area shown by the colored rectangles are used for the VR calculation.

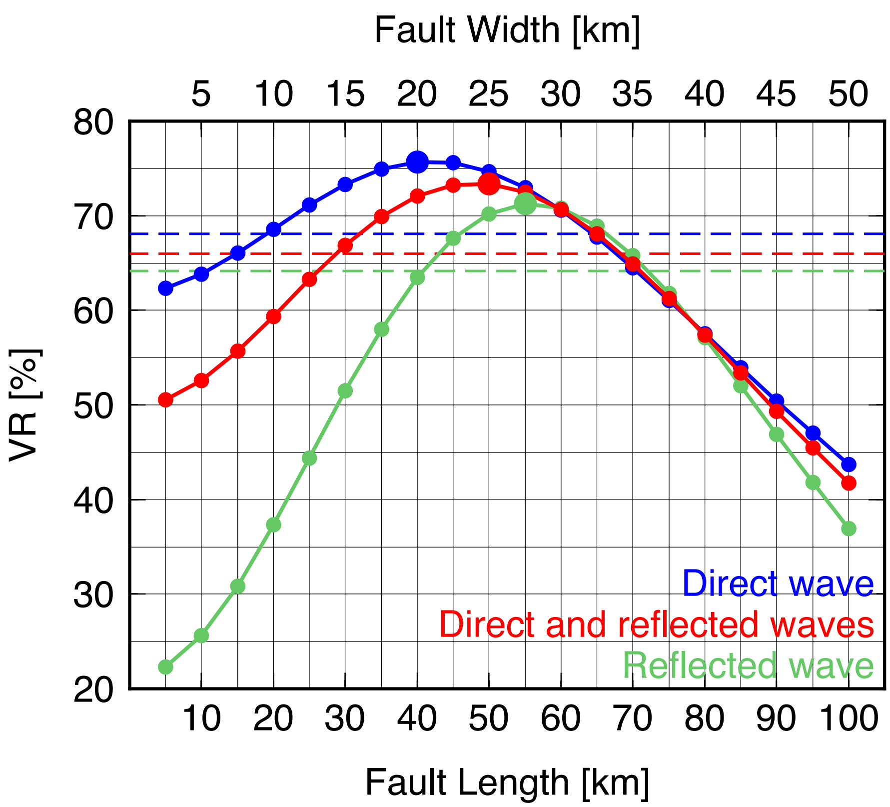

Figure 6. Result of the grid search for the fault dimension, using both direct and reflected waves (red), direct wave alone (blue), and coastal reflected wave alone (green). Note that tsunami was calculated using the LLW equation. Colored dashed lines denote the 90 % of the optimum VR for each analysis.

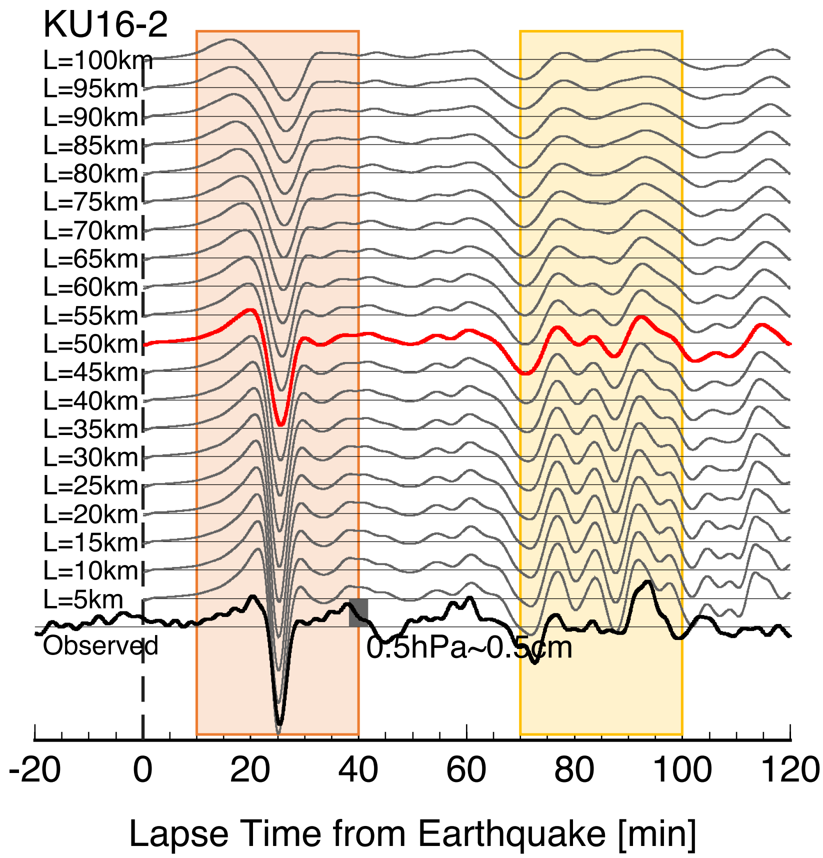

Figure 7. Comparison between the observed (thick black curve) and the calculated waveforms for different earthquake source lengths, at the station KU16-2. The waveform calculated from the optimum fault solution using both direct and reflected waves (L = 50 km) is shown in red.

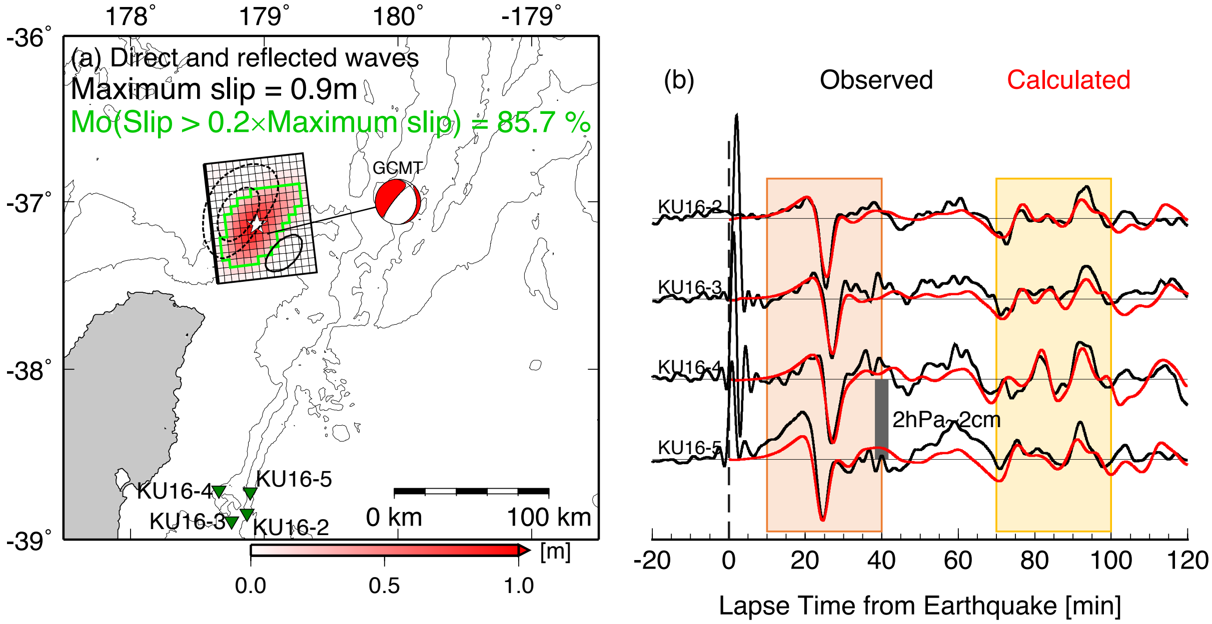

Figure 8. Result of the finite fault inversion using both direct and reflected waves. (a) Slip distribution on the fault (slip amount is represented by color scale). Contour lines denote vertical displacement calculated from the slip distribution (contour intervals are 5 cm). The star denotes the location of the centroid calculated from the fault model. The subfaults with slips larger than 20 % of the maximum slip are marked by right green lines. (b) Comparison of the waveforms between the observed (black) and calculated waveforms (red).

Journal of Geophysical Research: Solid Earth

Supporting Information for

Using tsunami waves reflected at the coast to improve offshore earthquake source parameters: Application to the 2016 Mw 7.1 Te Araroa earthquake, New Zealand

Tatsuya Kubota[1], Tatsuhiko Saito[1], Yoshihiro Ito[2], Yoshihiro Kaneko[3], Laura M. Wallace[3,4], Syuichi Suzuki[5], Ryota Hino[5], and Stuart Henrys[3]

[1]National Research Institute for Earth Science and Disaster Resilience, Tsukuba, Japan
[2]Disaster Prevention Research Institute, Kyoto Univesity, Uji, Japan
[3]GNS Science, Lower Hutt, New Zealand
[4]University of Texas Institute for Geophysics, Austin, Texas, USA
[5]Graduate School of Science, Tohoku University, Sendai, Japan

Contents of this file

Introduction

Text S1 describes the detail of the investigation of the reflected waves. Text S2 describes the method to estimate the time delay of tsunami arrival and the incident azimuth to the OBP array. Text S3 describes the evaluation test of the nonlinearity based on tsunami simulation. The method to calculate tsunami for the estimation of the centroid location and fault dimensions is described in Text S4. The detail of the finite fault inversion is described in Text S5. Comparison of the coastal tide gauges calculated from the CMT solutions are shown in Figure S1. Figure S2 shows the result of the tsunami simulation based on the USGS finite fault model. The simulation result based on the conjugate nodal plane from the GCMT solution is given in Figure S3. Figure S4 is the results of the tsunami simulation without the land. Figures S5 and S6 show the snapshots and the maximum tsunami height based on of the tsunami simulations, respectively. Result of the simulation with the modified bathymetry is in Figure S7. The ray tracing of the reflected waves is shown in Figure S8. Figure S9 shows the result of the array analysis of OBP data to extract tsunami incident azimuth. The comparison of the forward calculated waveforms based on LLW and NLL equations is in Figure S10. The result of tsunami simulation assuming Mw 8 earthquake is in Figure S11. Figure S12 is the result of ray tracing from the centroid locations obtained by grid search using the direct waves. Figure S13 shows the comparison between the observed waveform and the calculated waveforms from the different source length. Figure S14 shows the ABIC values used for the finite fault slip inversion. Figure S15 shows the results of the finite fault inversion. Distribution of the stress drop on the fault plane is shown in Figure S16.Tables S1 and S2 gives the time delay of tsunami arrival, for the direct and reflected waves, respectively. The raw OBP data used in this study is separately uploaded as Dataset S1.

Text S1

In order to investigate the where the coastal reflection radiated from, we show snapshots of the tsunami height distributions with and without the land (Figures S5a and S5b, respectively) and the distribution of the maximum absolute height (Figures S6a and S6b). We find that the main tsunami energy from the source is radiating to the middle part of the East Coast of the Raukumara Peninsula (Figures S6b). In order to retrieve the tsunami radiation associated with the coastal reflection, we calculate the difference between the tsunami height from the simulations with and without the land (Figure S5c) and its maximum height distribution (Figure S6c). We find that tsunami energy is trapped near the middle section of the East Coast of the Raukumara Peninsula (Figures S5c and S6c). These results suggest that the main energy from the reflected waves concentrates at the middle part of the East Coast of the Raukumara Peninsula.

We also conducted the additional tsunami calculation by modifying the bathymetry, in order to confirm that the coastal reflection occurred in the middle section of the East Coast of the Raukumara Peninsula (Figure S7). In the simulation, we modified the water depth shallower than 10 m to a constant depth of 10 m, but assigning land to each segment in turn; northern (Figure S7a1), middle (Figure S7a2), or southern (Figure S7a3). The simulation result assuming that the land exists only at the middle part of Raukumara Peninsula (red lines in Figure S7b2) reproduced the reflected waves at ~ 90 min well, and the simulations assuming the other part of the Raukumara Peninsula (blue lines in Figure S7b1 and green lines in Figure S7b3) did not explain the reflected waves at ~ 90 min (although the waves at ~ 70 min are reasonably explained). This result supports the idea that the coastal reflection mainly occurred at the middle section of the East Coast of the Raukumara Peninsula.

We then undertook the ray tracing of the coastal reflected tsunami waves (Figures 4 and S8). In the ray tracing, we assumed the reflection points at the middle part of the East Coast of the Raukumara Peninsula. In order to calculate the ray path, we used the pseudo-bending method proposed by Um and Thurber (1987). In this approach, the starting point and the ending point of the ray path are assumed, and the optimum ray path is searched so that the travel time between two points is minimized. In the calculation, we separately calculated the ray path: one is between the source and the coastal reflection point, and the other is between the reflection point and the OBP. We assumed three source locations, (1) at the maximum subsidence of the initial sea surface height distribution calculated based on the GCMT solution (Figures 4 and S7a), (2) at the GCMT centroid (Figure S7b), and (3) at the maximum uplift based on the GCMT solution (Figure S7c). Most of the ray paths are almost the same regardless of the assumed source location, but the travel times take slightly longer when the source is assumed at the maximum subsidence (~ 85 – 90 min). Considering that the main phases of the reflected waves are observed at ~ 90 min, the reflected waves are mainly generated by the subsidence of tsunami source. Furthermore, we also calculated the ray paths directly propagating from the source to the OBP (dashed lines in Figure S5). The travel time calculated of the direct tsunami is 25.4 min when the source is assumed at the maximum subsidence, which is consistent with the observed travel time (Table 2).

Text S2

The peak timing of direct and reflected tsunami waveform arrivals (Table 2, noted by small dots in Figure 1c) are slightly different between the OBP stations. By using the time delay between the two OBPs, we can estimate the approximate incident azimuth of the direct and reflected tsunamis. We calculated the time delay of tsunami arrivals between the two OBPs by calculating the cross correlation between *i*th and *j*th OBPs (CC_{ij}), defined as:

$$\mathrm{CC}_{ij} = \frac{\sum_k [u_i(k\Delta t)u_j(k\Delta t+\tau)]}{\sqrt{\sum_k u_i(k\Delta t)^2}\sqrt{\sum_k u_j(k\Delta t+\tau)^2}}, \quad \text{(S1)}$$

where $u_i(t)$ denotes the waveform of the *i*th OBP at $t = k\Delta t$, Δt is the data sampling interval (1 s), and τ is the lag time between the two waveforms. We estimated the time delay between the *i*th and *j*th stations (τ_{ij}^{obs}) for the direct wave (10 – 40 min, Table S1) and the reflected wave (70 – 100 min, Table S2), by calculating the lag time τ which maximize the CC_{ij}.

As a result, the first direct tsunami arrival (~ 25 min) occurs at the northeastern-most station KU16-5, and then arrives at station KU16-2 < 1 min later. Tsunami arrivals are recorded last at the western stations KU16-3 and KU16-4 almost at the same time, ~ 2 min after the first arrival at KU16-5. This suggests that the first tsunami propagated from the northeast/east-northeast of our OBP array. The secondary tsunami arrives first at KU16-5, and is earlier by ~ 1.5 min at the northern stations (KU16-4 and KU16-5) compared to the southern stations (KU16-2 and KU16-3). This suggests that the secondary tsunamis propagated from the north-northeast. We also show the time delay estimated from the timing of the secondary tsunami in Table S2. The lag times estimated from the direct waves are almost identical to those calculated from the peak timing, but those from the reflected waves are different between the cross correlation and peak timing. This suggests that the reflected waves are more complex than the direct waves, probably because the complex coastal bathymetry distort the waveforms in addition to the travel time change.

After estimating the time delay, we then estimate the incident azimuth of the tsunami arrivals based on array analysis. Based on the plane wave approximation, the time delay between the *i*th and *j*th stations ($\tau_{ij}^{cal}(\mathbf{s})$) can be expressed as:

$$\tau_{ij}^{\mathrm{cal}}(\mathbf{s}) = \mathbf{s} \cdot (\mathbf{x}_j - \mathbf{x}_i), \quad \text{(S2)}$$

where $\mathbf{s} = (s_x, s_y)$ is the slowness vector and $\mathbf{x}_i = (x_i, y_i)$ is the location of the *i*th station. We search for the optimum slowness vector, which minimizes the root mean square (RMS) misfit of the time delay (RMS(**s**)), defined as:

$$\mathrm{RMS}(\mathbf{s}) = \sqrt{\frac{1}{N}\sum_{i<j}\left(\tau_{ij}^{obs} - \tau_{ij}^{cal}(\mathbf{s})\right)^2}, \quad \text{(S3)}$$

where τ_{ij}^{obs} is the time delay obtained from the observed tsunami waveform (Tables S1 and S2).

The estimated incident azimuths for the direct and reflected tsunamis are 71° and 29°, respectively (Figure S9), which is consistent with those expected from the time delay. We also calculate the water depth expected from the optimum slowness, based on the linear long wave theory:

$$H = \frac{v^2}{\mathrm{g}_0} = \frac{1}{\mathrm{g}_0 s^2}, \quad \text{(S4)}$$

where $s = |\mathbf{s}| = \sqrt{s_x^2 + s_y^2}$. Using the direct wave, we obtain *H* = 1771 m, which is almost equivalent to the average water depth around the OBP array. We also obtain *H* = 4360 m from the reflected waves, which is much deeper than the average depth. This is probably due to the complexity of the reflected waves, including the travel time change caused by bathymetry changes along the coast.

Text S3

In general, nonlinearity should be considered to accurately model tsunami propagation near the coast (e.g., Satake, 1995; Saito et al., 2014), whereas nonlinear effects are very small when tsunami propagate in the deep ocean. Therefore, we additionally conducted tsunami calculation considering the nonlinearity. We used the nonlinear long wave (NLL) equation (e.g., Satake, 1995; Saito et al., 2014), imposing a bottom friction with Manning's coefficient of n = 0.03 ($m^{-1/3}$ s). We also included the tsunami inundation in our calculation, as a moving boundary condition between the land (dry cell) and sea (wet cell) The other details of the NLL tsunami calculation scheme is described in Saito et al. (2014). The other settings were all the same as the simulation using the LLW equation.

We show a comparison of the calculated tsunami waveforms using the NLL equations in Figure S10. The waveforms from the LLW (red) and NLL (blue) equations are very similar, not only for the direct waves but also for the reflected waves. In order to evaluate the agreement between the model waveforms, we calculate the variance reduction (VR_{cal}), using the following equation:

$$\mathrm{VR_{cal}} = \left(1 - \frac{\sum_i^N \left(u_i^{\mathrm{A}} - u_i^{\mathrm{B}}\right)^2}{\sum_i^N \left(|u_i^{\mathrm{A}}| \times |u_i^{\mathrm{B}}|\right)}\right) \times 100\ (\%), \qquad \text{(S5)}$$

where u_i^{A} and u_i^{B} is the i-th data of the calculated waveforms A and B, respectively, and N denotes the number of data used for the calculation. VR_{cal} for four OBP waveforms between from LLW equation and from NLL equations using a time window of 0 – 60 min and 60 – 120 min are 100 % and 98.5 %, respectively. This suggests that the nonlinearity is small in this situation.

We also conducted additional tsunami simulations using a finer grid spacing (Δx = Δy = 250 m) compared to the original calculation (Δx = Δy = 500 m) (Figure S10). As a result, even if we use the finer grid spacing of 250 m, the difference between the calculated waveforms using the LLW and NLL equations is small (i.e., the nonlinearity is very small). We also compare the simulation result using a grid spacing of 500 m with that using a finer grid spacing (250 m). Overall, the calculated OBP waveforms are similar between the simulations using the grid spacing of 500 m and the finer 250 m spacing, although the waveforms at the coastal station, East Cape, varied slightly. This suggests the offshore OBP waveforms are less affected by the complex coastal bathymetry, than the coastal tide gauges.

We find that the effect from nonlinearity is small in the reflected waves observed by the OBP array. This is probably because of the moderate magnitude and small tsunami amplitude at the coast. To illustrate this, we conduct additional tsunami simulations, by assuming an earthquake with larger magnitude (Mw 8.0) which generates a much larger tsunami (Figure S11). In this calculation, we assumed the magnitude of Mw 8.0, and estimated the fault length and width, and slip amount, D, based on the scaling law (L = 132 km, W = 46km, D = 5.2 m). We used the strike, dip, rake and centroid location of the GCMT solution (Figure S11a). As a result, the direct waves are the same between those calculated by using the LLW (red) and NLL (blue in Figure S11b) equations, because the direct waves propagate in the deep ocean. But the reflected waves, which propagate near the shallow area, are slightly different. The VR_{cal} between the waveforms calculated by the LLW and NLL equations, using the time window of 0 – 60 and 60 – 120 min was 100 % and 92.9 %, respectively. VR_{cal} for the reflected waves is lower than that from the original (Mw 7.1) result, suggesting that effects of nonlinearity at the coast cannot be neglected in the larger earthquake.

Text S4

For the estimation of the centroid location and the fault dimensions, the tsunami is calculated based on a linear superposition of pre-computed tsunami Green's functions from small source elements for seafloor displacement (unit tsunami sources). This method is proposed by Kubota et al. (2015), in order to minimize the tsunami calculation time. We distributed 39× 39 unit sources in the area 400 km × 400 km around the focal area. We use pyramid-like-shaped unit sources with dimensions of 20 km × 20 km, identical to those used in Kubota et al. (2015). Each has a horizontal spacing of 10 km, and overlaps with the neighboring ones. After the calculation of tsunami from each unit source, we apply a bandpass filter similar to that applied to the observed records, to obtain the tsunami Green's function. After calculating the seafloor deformation using the equations of Okada (1992), the deformation is expressed by a linear superposition of the unit sources. Then tsunami was calculated by a linear superposition of the tsunami Green's function.

Text S5

In the finite fault slip inversion, we assumed the rectangular planar fault with the size of 80 km length and 70 km width, which is determined based on the optimum fault dimension obtained by the grid search analysis. The center of the rectangular planar fault coincides with the point 178.97°E, 37.10°S, and 27.8 km depth, which is the optimum fault center location obtained by the grid-search of the fault horizontal location. We used the fault geometry from the GCMT solution (strike = 354°, dip = 20°, and rake = –134°). We calculated the seafloor vertical deformation from each subfault by using the equation of Okada (1992). We assumed that the sea surface vertical displacement is equal to the seafloor vertical deformation. Tsunami Green's functions for the finite slip inversion from each subfault was calculated by the superposition of the tsunami Green's function of the tsunami source (described in Text S4).

In the finite fault inversion, we assumed the observed tsunami waveforms can be expressed as a superposition of the tsunami Green's function from each subfault. The observation equation is expressed as:

$$\begin{pmatrix}\mathbf{d}\\ \mathbf{0}\end{pmatrix} = \begin{pmatrix}\mathbf{G}\\ \alpha\mathbf{S}\end{pmatrix}\mathbf{u}, \tag{S6}$$

where **d** is a vector composed of the tsunami data, **G** is a matrix composed of the tsunami Green's function for the finite slip inversion, and **u** is a vector representing the slip distribution of the fault, which are we want to obtain. A matrix **S** denotes the smoothing constraint of the fault slip, and α is the weighing of the smoothing constraint.

The weighting of the smoothing constraint was set as $\alpha = 5$, which was determined based on the value of Akaike's Bayesian Information Criterion (ABIC) (Yabuki and Matsu'ura, 1992) (Figure S14).

We also calculated the location (longitude and latitude) of the centroid ($\mathbf{x}_g = (x_g, y_g)$) from the finite fault model, using the following equation:

$$\mathbf{x}_{\mathrm{g}} = \sum_{i=1}^{N} \frac{\mathbf{x}_i \times a_i}{a_i}, \tag{S7}$$

where N denotes the number of the subfaults included in the main rupture area, and $\mathbf{x}_i = (x_i, y_i)$ is the location of the center of the ith subfault included in the main rupture area and a_i is the slip amount of the ith subfault.

We then calculated the shear stress (i.e., the stress drop) distribution, using the equation of Okada (1992), by computing the shear stress change at the center of each subfault (Figure S16). We also calculated the energy-based stress drop $\Delta\sigma_E$ (e.g., Noda et al., 2013; Ye et al., 2016), expressed as:

$$\Delta\sigma_E = \frac{\int_\Sigma \Delta\sigma_1 \Delta u_1 dS}{\int_\Sigma \Delta u_1 dS}, \tag{S8}$$

where $\Delta\sigma_1$ and Δu_1 are the distributions of the stress drop and slip amount on the slip area. This equation can be simplified as:

$$\Delta\sigma_E = \frac{\sum_{i=1}^{N} \Delta\sigma_i u_i}{\sum_{i=1}^{N} u_i}, \tag{S9}$$

where $\Delta\sigma_i$ and u_i are the stress drop and slip amount of ith subfault. Using the stress drop and slip amount of all subfaults, we obtain $\Delta\sigma_E$ as 0.8 MPa. If we use the subfaults inside the main rupture area (marked by green rectangles in Figure 8), we obtain $\Delta\sigma_E$ as 1.0 MPa.

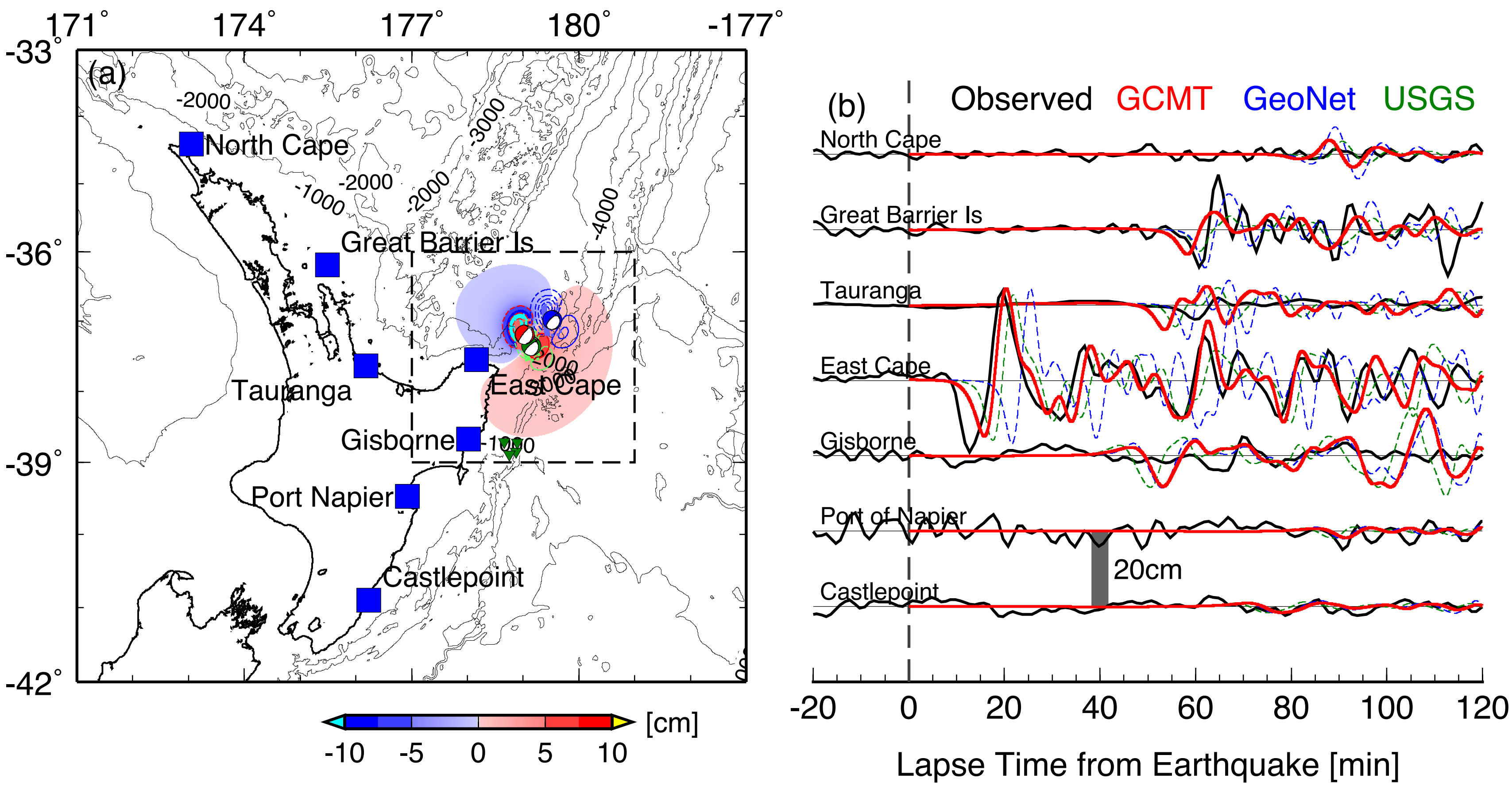

Figure S1. (a) Location map of the coastal tide gauges. Background colors (red and blue) show the initial tsunami height distribution from the GCMT solution. Colored rectangles denote the fault models calculated from the CMT solutions. The black dashed lines denote the area shown in Figure 2a. (b) Comparison of the forward-calculated waveforms of the coastal tide gauges (trace colors match the corresponding fault models used in (a)).

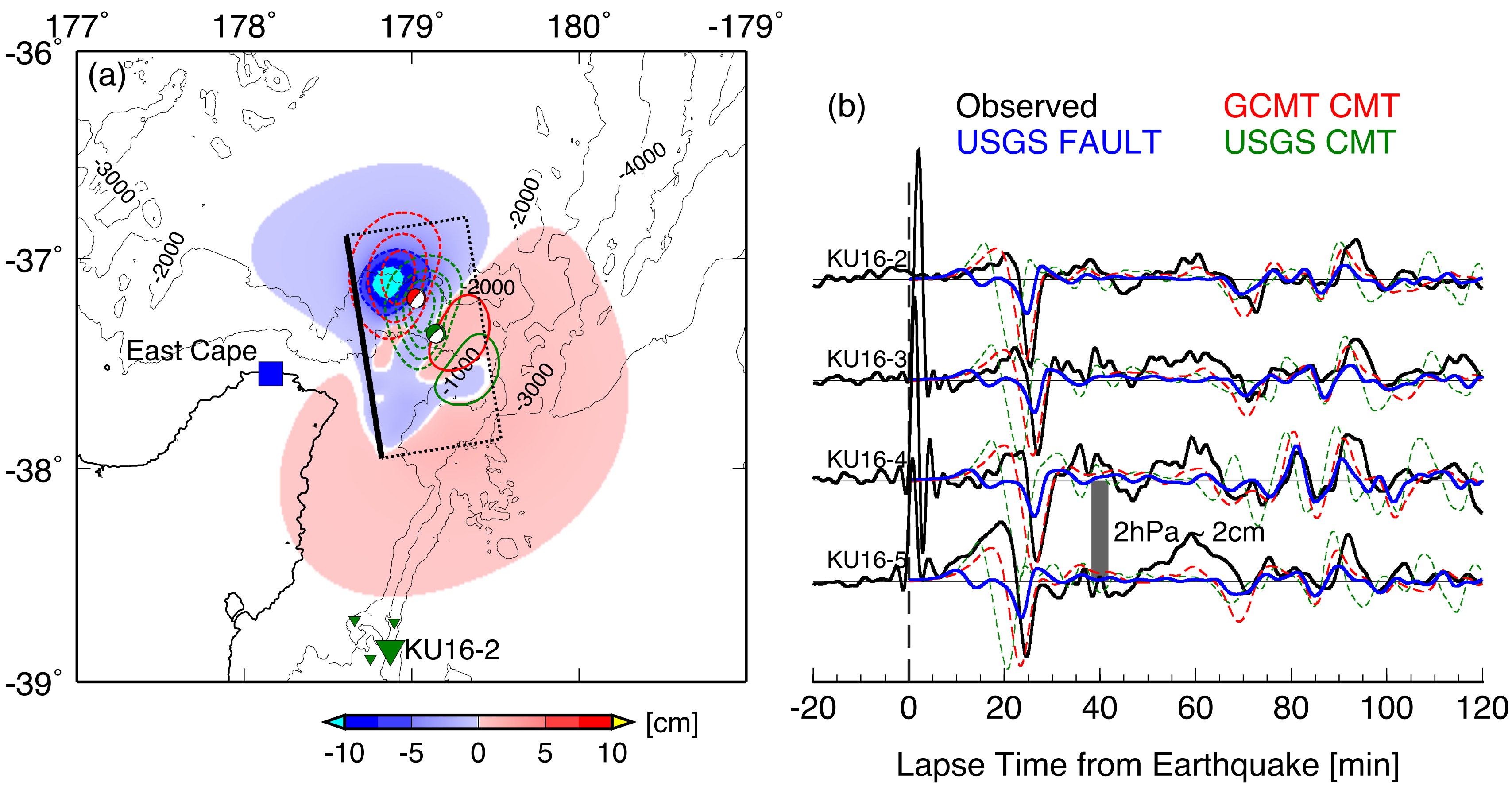

Figure S2. (a) Initial tsunami height distributions calculated from the finite fault model from the teleseismic analysis by USGS (https://earthquake.usgs.gov/earthquakes/eventpage/us10006jbi#finite-fault). Back ground colors (red and blue) show the initial tsunami height distribution calculated from the USGS finite fault model. The black rectangle and contour lines denote the fault models and tsunami source distribution (contour intervals are 5 cm). (b) Comparison of the forward-calculated waveforms from the rectangular model based on the GCMT solution (red), the USGS finite fault model (blue), and the rectangular model based on the USGS solution (green), with the observed waveform (black).

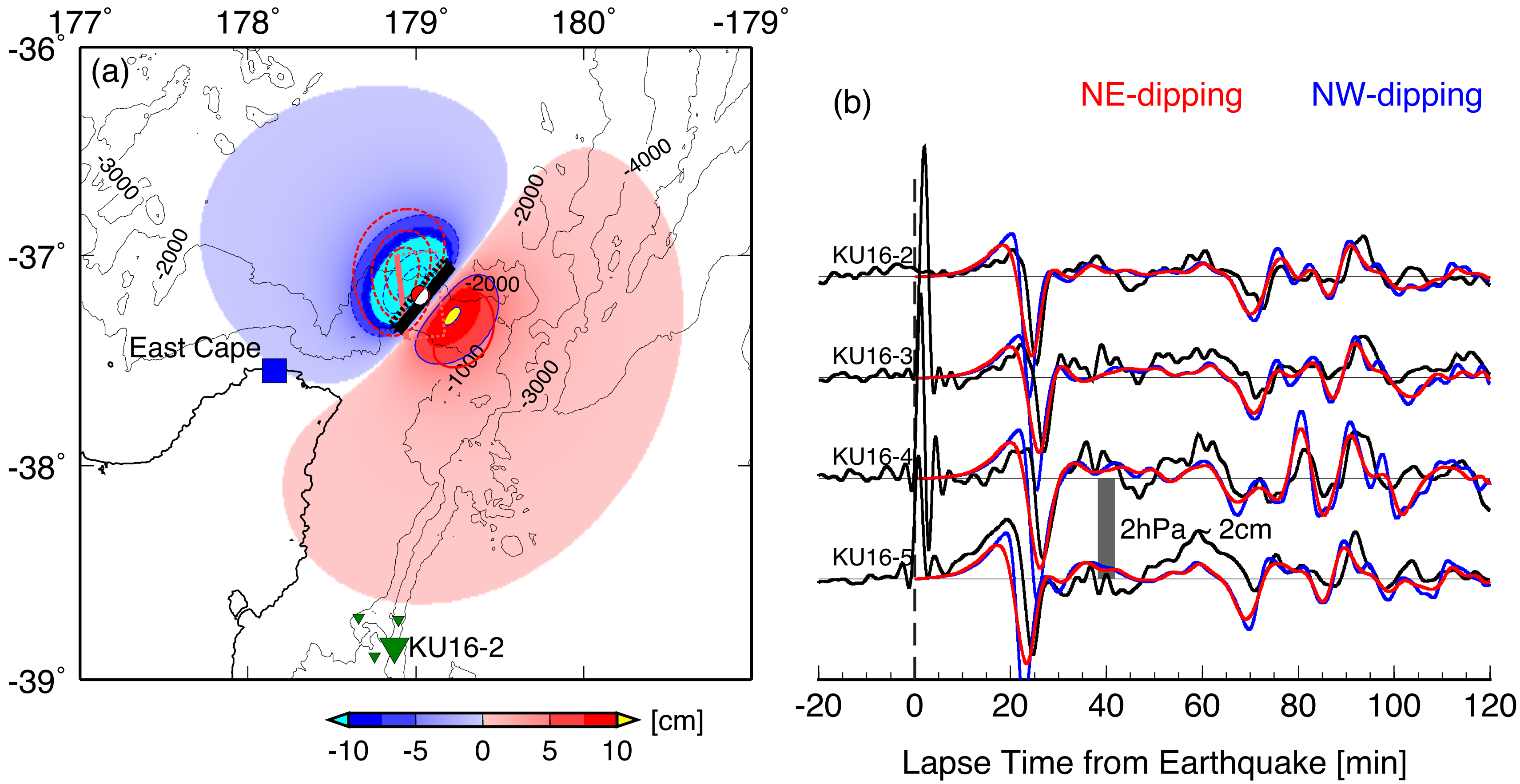

Figure S3. (a) Initial tsunami height distributions calculated from the GCMT solution, assuming the northwest-dipping nodal plane (strike = 220°). Background colors (red and blue) show the initial tsunami height distribution. The black and red rectangles denote the fault models calculated from the northwest-dipping (strike = 220°) and north-east dipping (strike = 354°) planes, respectively. (b) Comparison of the forward-calculated waveforms from the northwest-dipping (blue) and northeast-dipping (red) nodal planes.

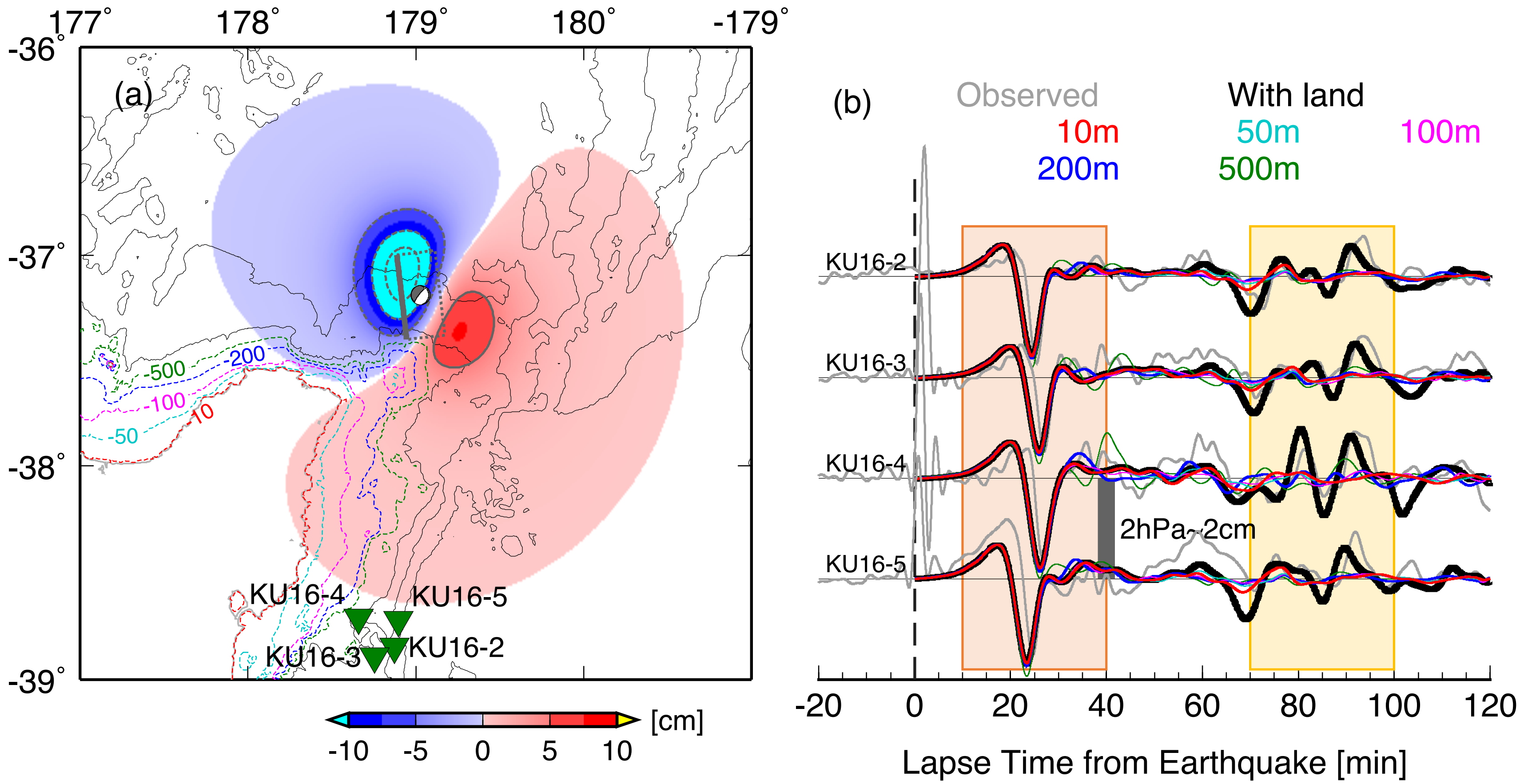

Figure S4. Comparison of the observed (gray) and calculated waveforms based on the GCMT solutions, with (black) and without the land. In the calculation that excludes land, we modified the water depth in the shallow region to a constant depth of 10 m (red), 50 m (light blue), 100 m (pink), 200 m (blue), and 500 m (green). The iso-depth contours from the true bathymetry are noted by the dashed lines.

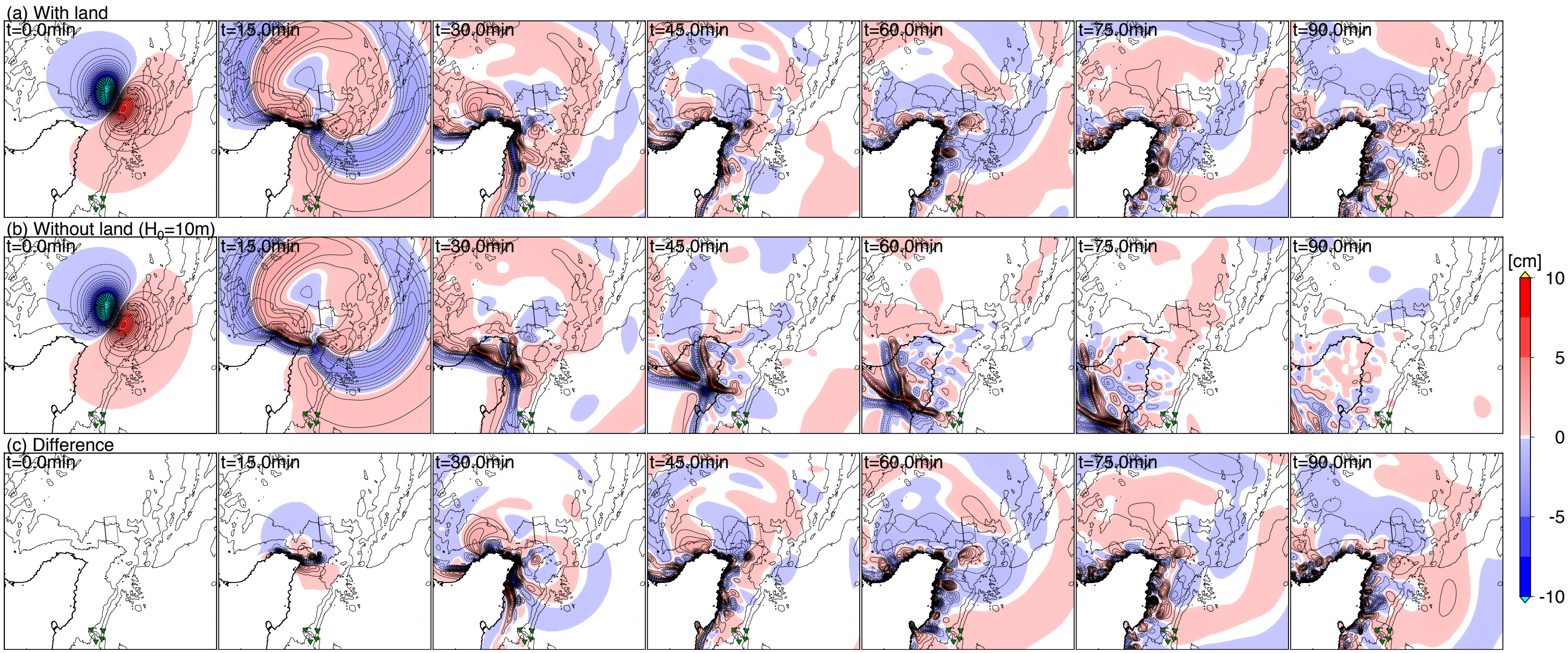

Figure S5. Snapshots for the tsunami height from (a) the simulation with the original bathymetry data, (b) the simulation without the land (< 200 m), and (c) the difference between the simulation with and without the land. Contours are drawn at 0.5 cm intervals.

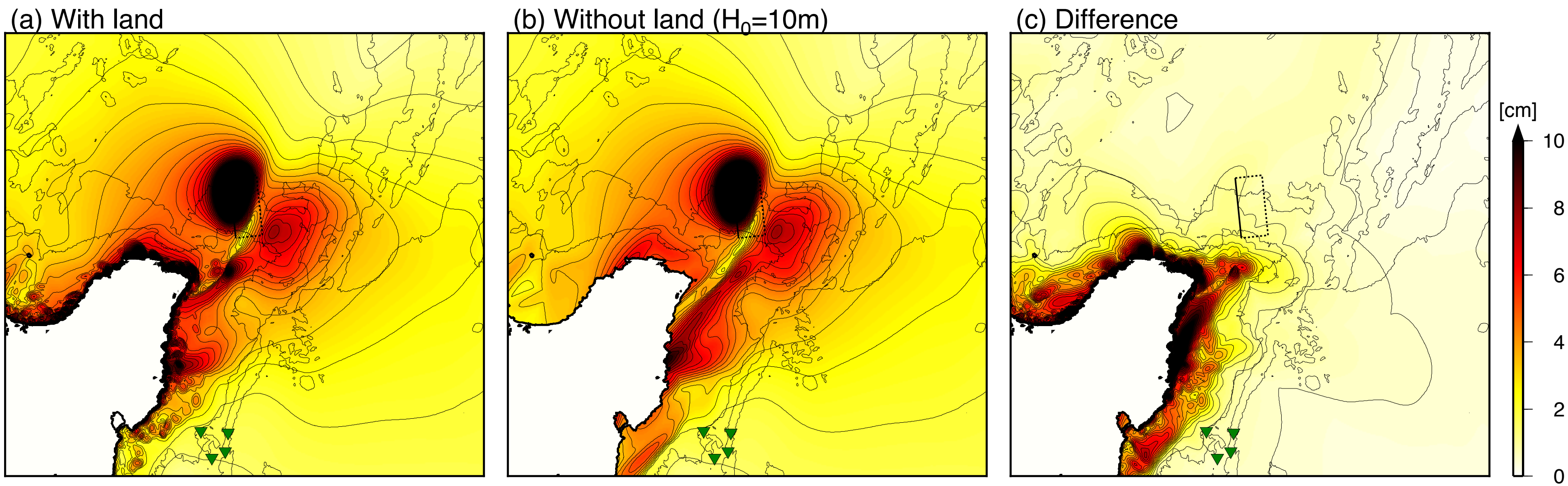

Figure S6. Distributions of the absolute maximum value of tsunami height, calculated from (a) the simulation with the original bathymetry data, (b) the simulation with the modified bathymetry data (water depth shallower than 200 m is modified to a constant depth of 200 m), and (c) the difference between these two simulations. The contours are drawn at 0.5 cm intervals.

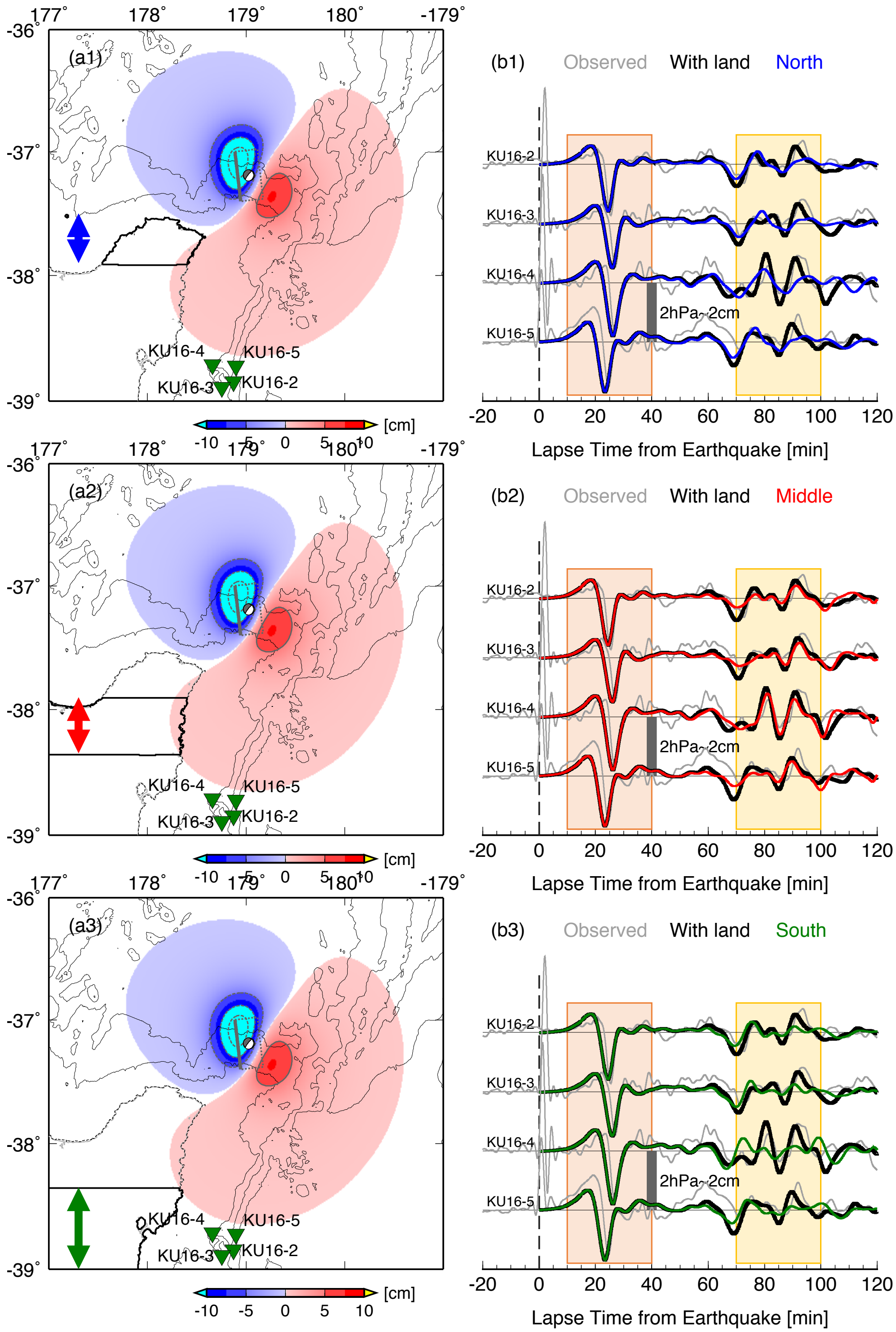

Figure S7. Result of the tsunami calculation with the modified bathymetry, assigning the land to the (a1) northern, (a2) middle, and (a3) southern segments of the Raukumara Peninsula. The 10 m iso-depth contour are noted by the dashed line. The black lines denote the area with the land assigned. The other segments are modified to a constant water depth of 10 m. (b1, b2, b3) Comparison of the observed (gray) and calculated waveforms based on the GCMT solutions, using the original bathymetry (black) and the modified bathymetry (colored).

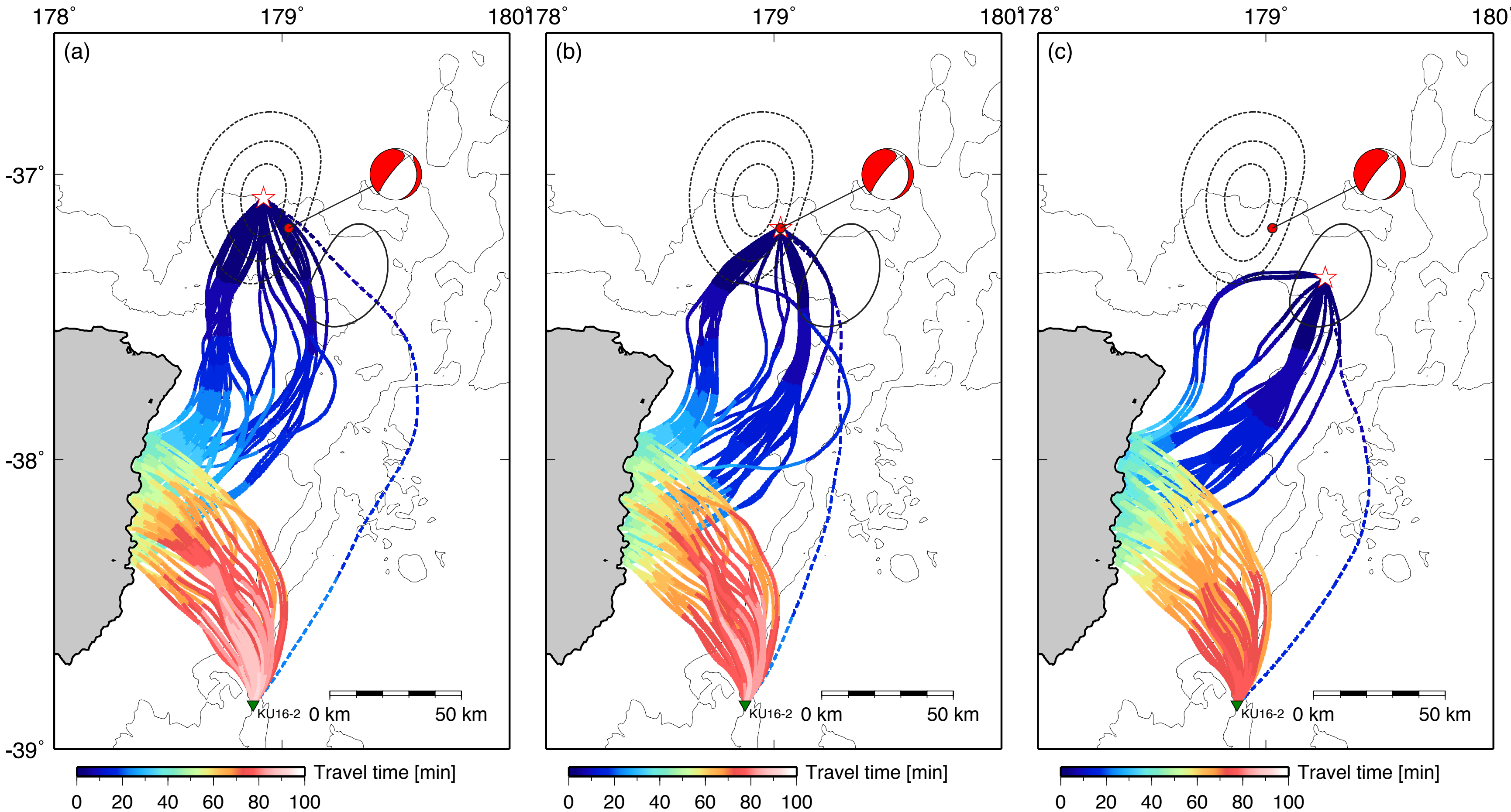

Figure S8. Ray tracing of the coastal reflected tsunami waves, assuming a source at (a) the maximum subsidence expected from the GCMT solution, (b) the GCMT centroid, and (c) the maximum uplift expected from the GCMT solution. Red star denotes the location of the assumed source. The dashed lines denote the ray paths of the direct tsunami waves. Colors of the rays of the reflected tsunami waves denote the travel time from the source.

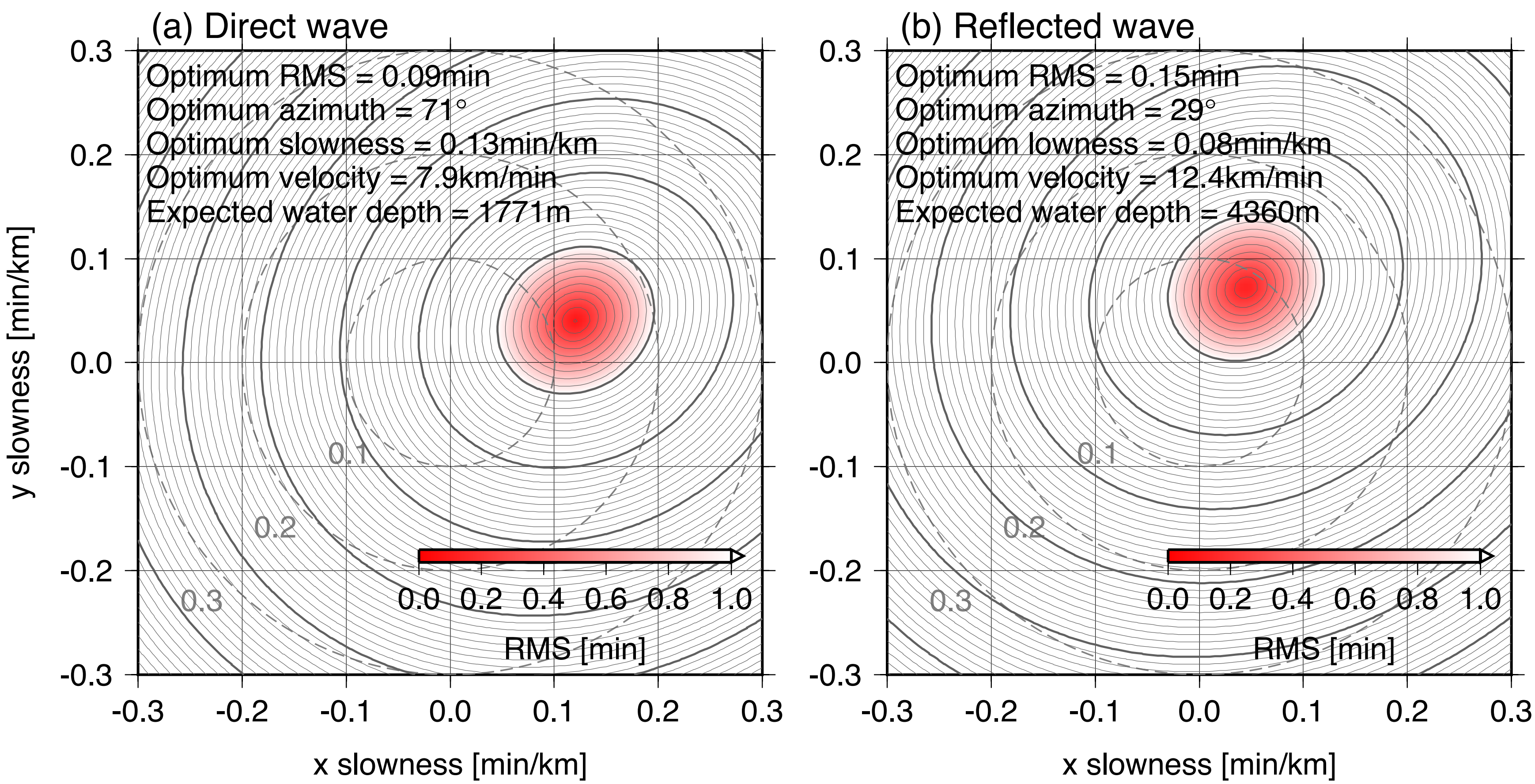

Figure S9. Distribution of the RMS(**s**) for (a) direct wave and (b) reflected waves. Color and solid contour lines denote the RMS(**s**) value. Thin and thick contour lines are drawn by 0.1 and 1 min intervals, respectively. Dashed circles denote the iso-slowness lines with 0.1 min/km intervals.

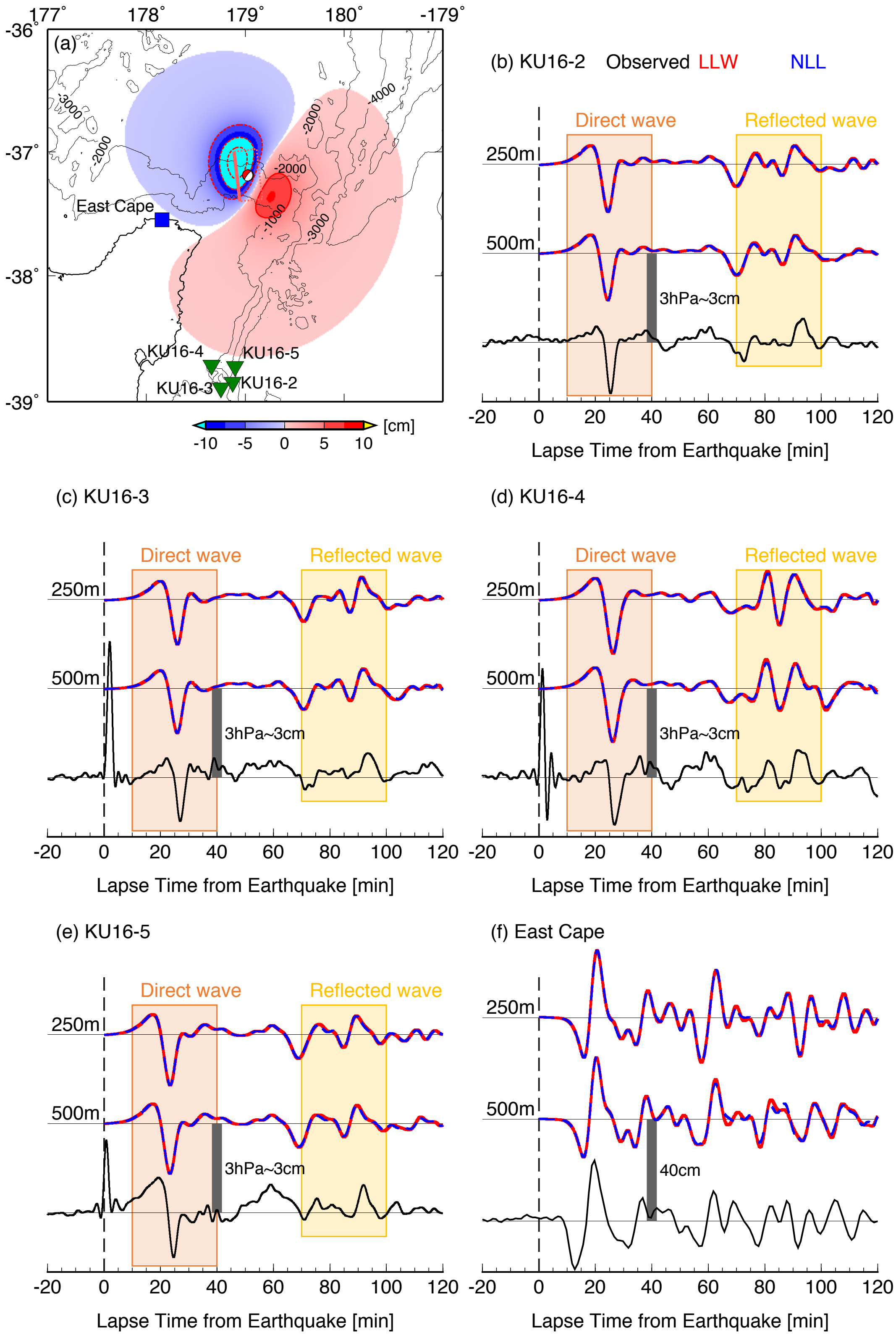

Figure S10. Comparison of the forward calculated waveforms based on the Global CMT solution using the LLW (red) and NLL (blue) equations, with the computational grids of 500 and 250m.

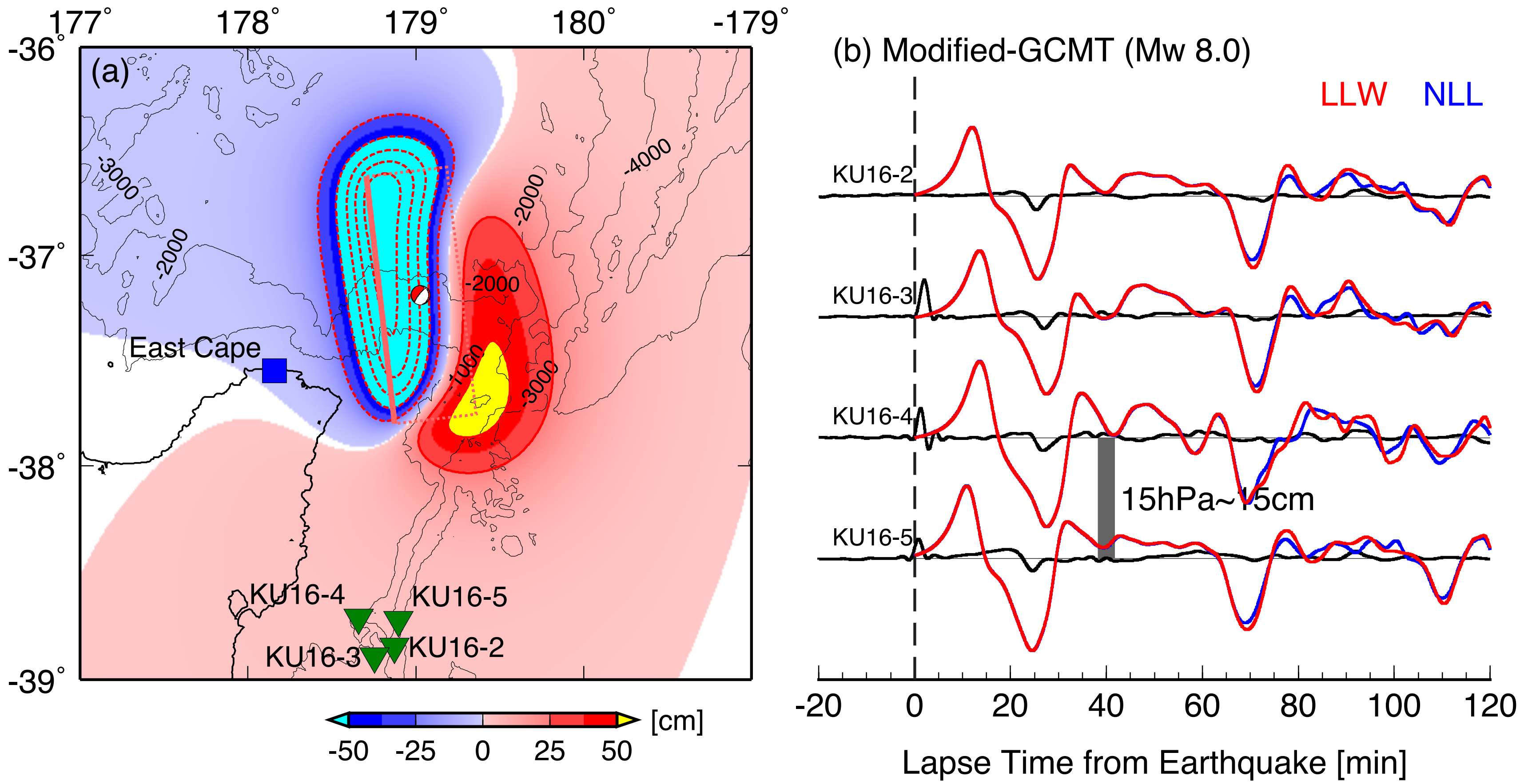

Figure S6S11. (a) Tsunami source distribution calculated from the modified GCMT solutions, which has a magnitude comparable to an Mw 8.0. (b) Comparison of the forward calculated waveforms based on the CMT solutions at the OBPs from LLW (red) and NLL (blue) equations. The observed pressure waveforms associated with the Te Araroa earthquake is also shown by black lines.

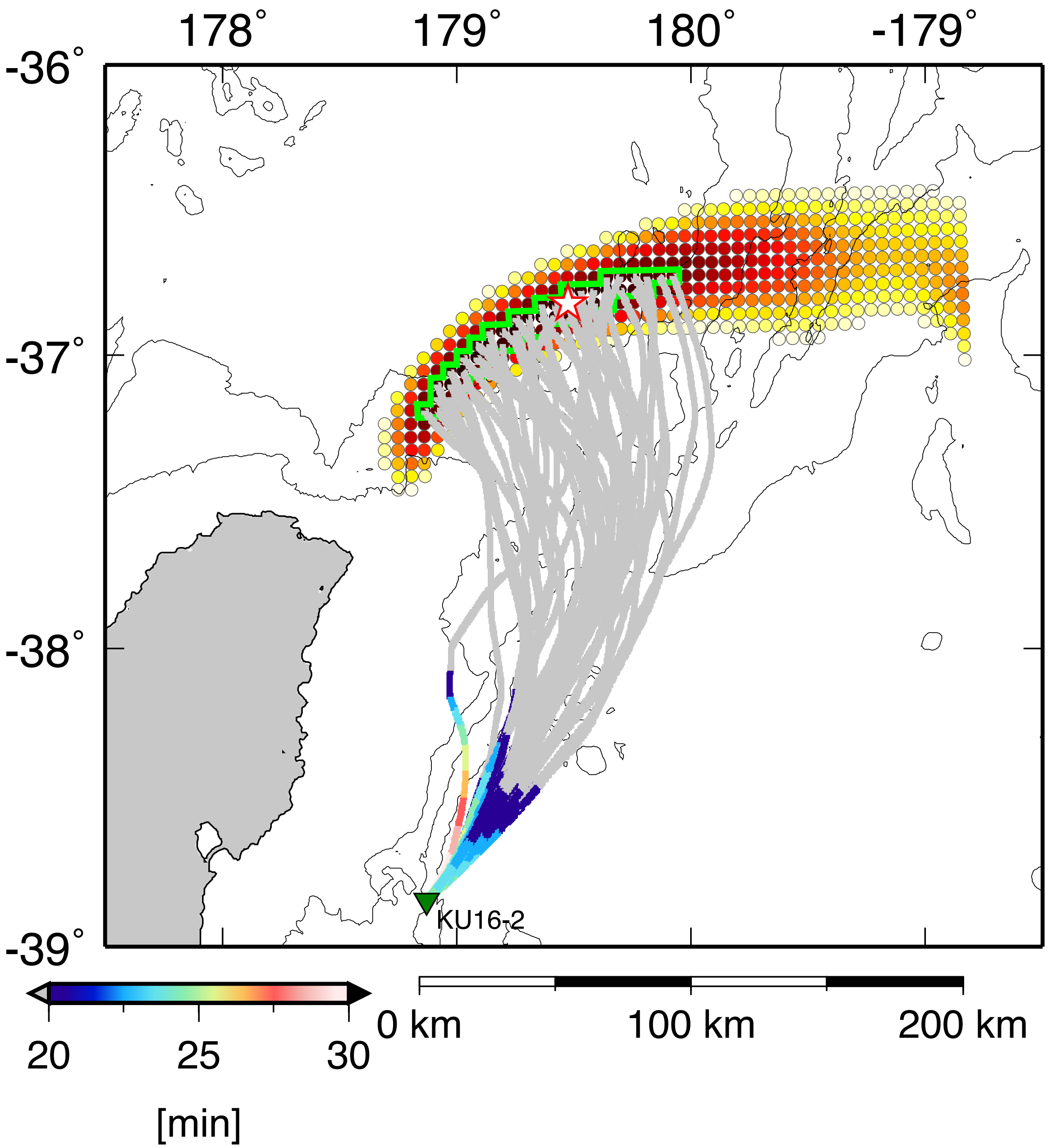

Figure S12. Result of the ray tracing from the solutions in the high-variance reduction (VR) area, obtained by the direct waves alone (small green circles) to the OBP station KU16-2. The red star denotes the optimum solution obtained from the direct waves.

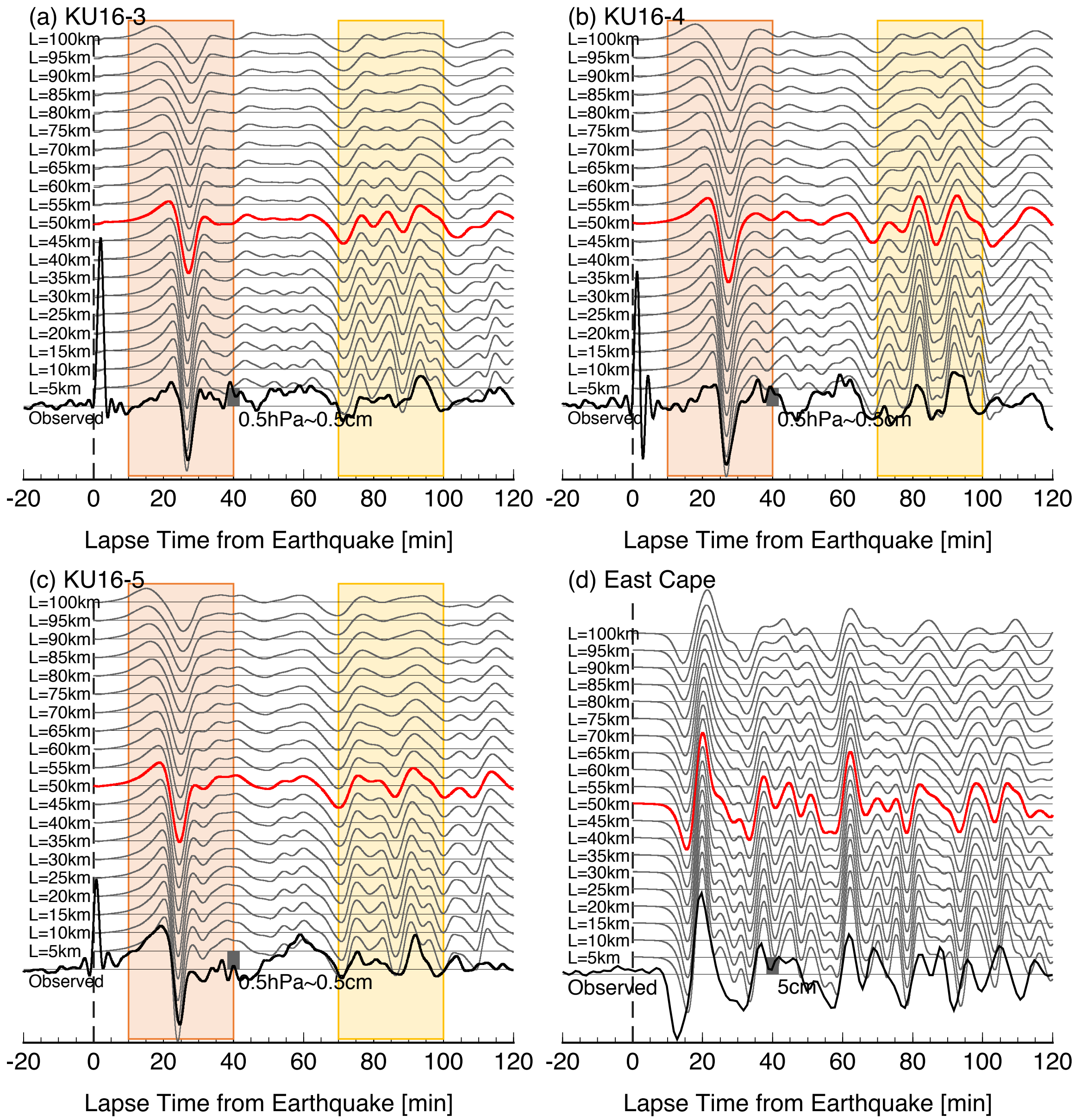

Figure S13. Comparison between the observed (thick black curve) and the calculated waveforms from the different source length, at the stations (a) KU16-3, (b) KU16-4, (c) KU16-5, and (d) East Cape. The waveforms calculated from the optimum fault solution using both direct and reflected waves (L = 50 km) are shown in red.

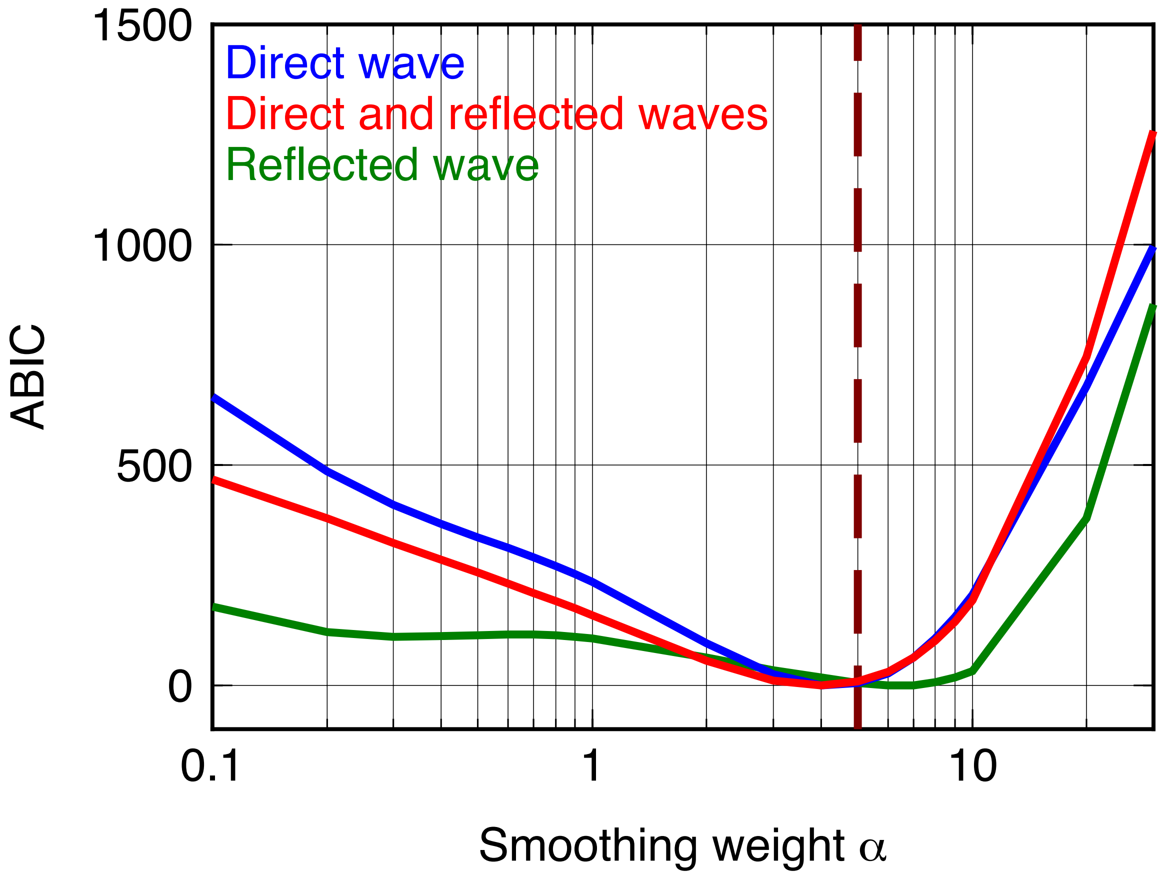

Figure S14. Values of ABIC for the finite fault inversion using the direct waves alone (blue), the reflected waves alone (green), and both direct and reflected waves (red), plotted as a function of α. We adopted the smoothing weight of α = 5, denoted by the dashed line.

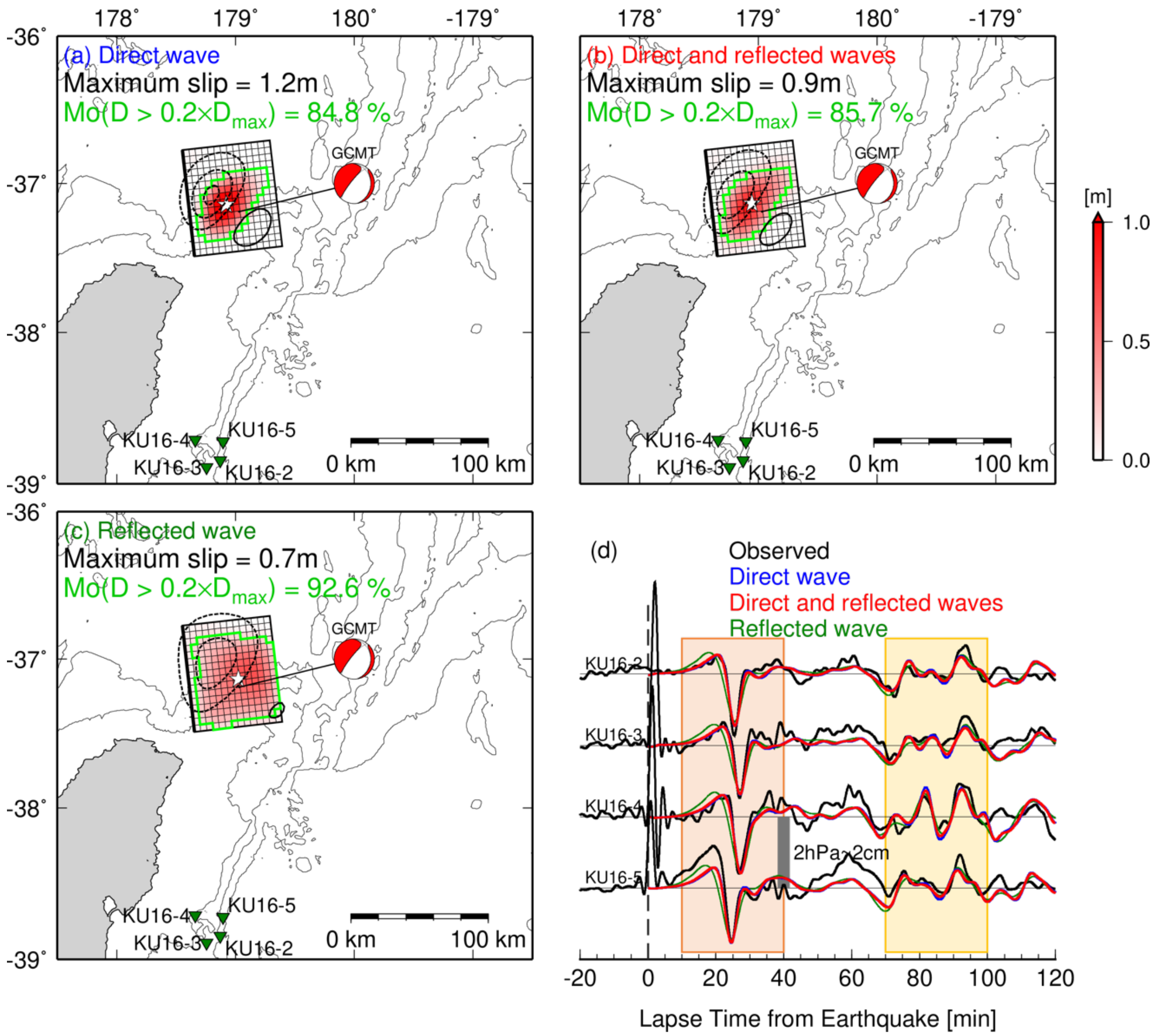

Figure S15. Results of the finite fault inversion, using (a) the direct waves alone, (b) both direct and reflected waves, and (c) the reflected waves alone. (a–c) Slip distribution on the fault (slip amount is represented by color scale). Contour lines denote vertical displacement calculated from the slip distribution (contour intervals are 5 cm). The star denotes the location of the optimum centroid location obtained by the grid-search for the horizontal fault location. The subfaults with slips larger than 20 % of the maximum slip are noted by right green lines. The GCMT solution is also shown. (d) Comparison of the waveforms between the observed (black) and calculated waveforms from direct waves alone (blue), both direct and reflected waves (red), and reflected waves alone (green), for each OBP station. The area shown by colored rectangle is used for the inversion.

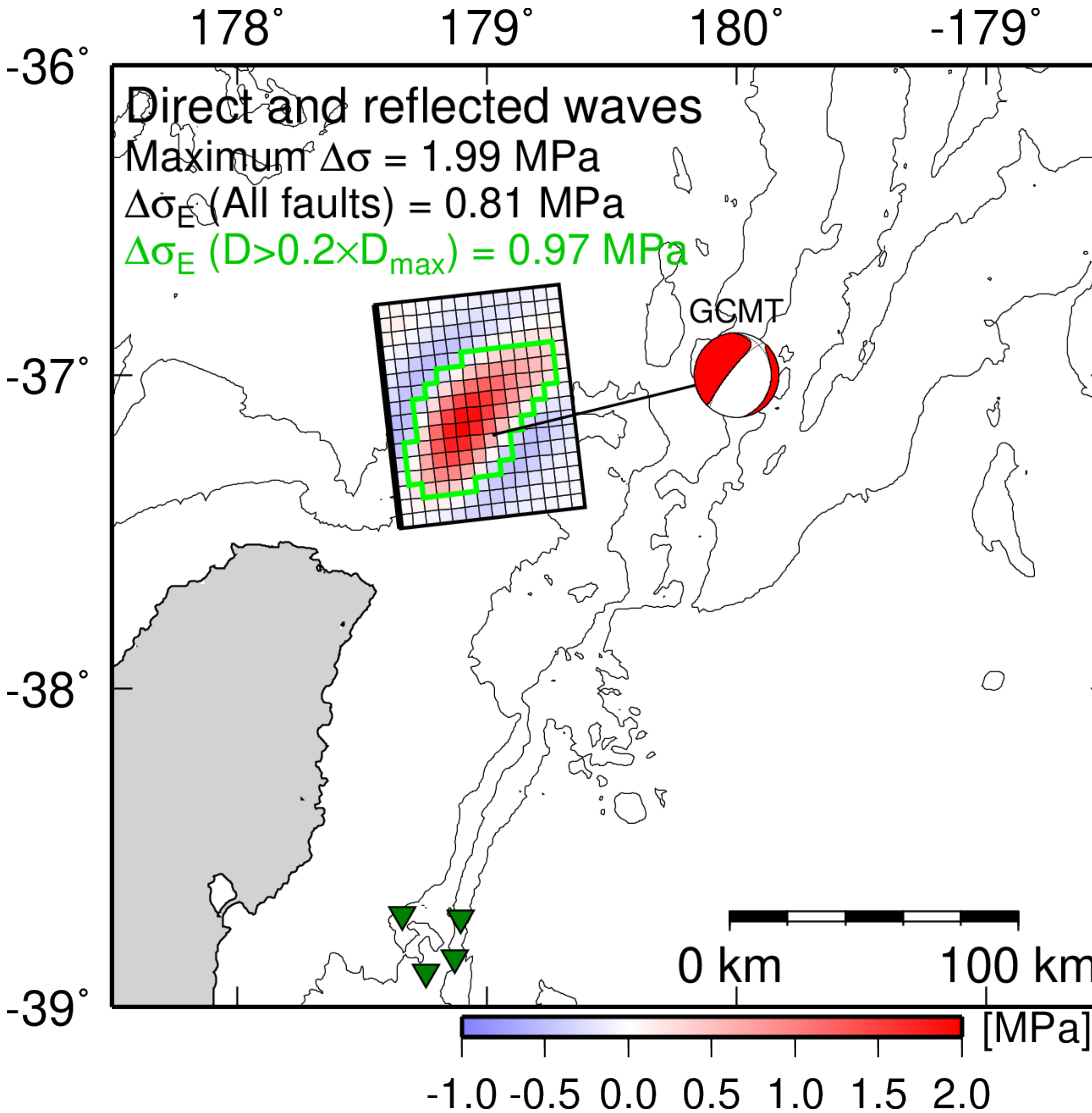

Figure S16. Distribution of shear stress change calculated from the finite fault model using both the direct and reflected waves (Figure 8). Positive value means the shear stress was reduced after the earthquake. The subfaults with slips larger than 20 % of the maximum slip are noted by right green lines.

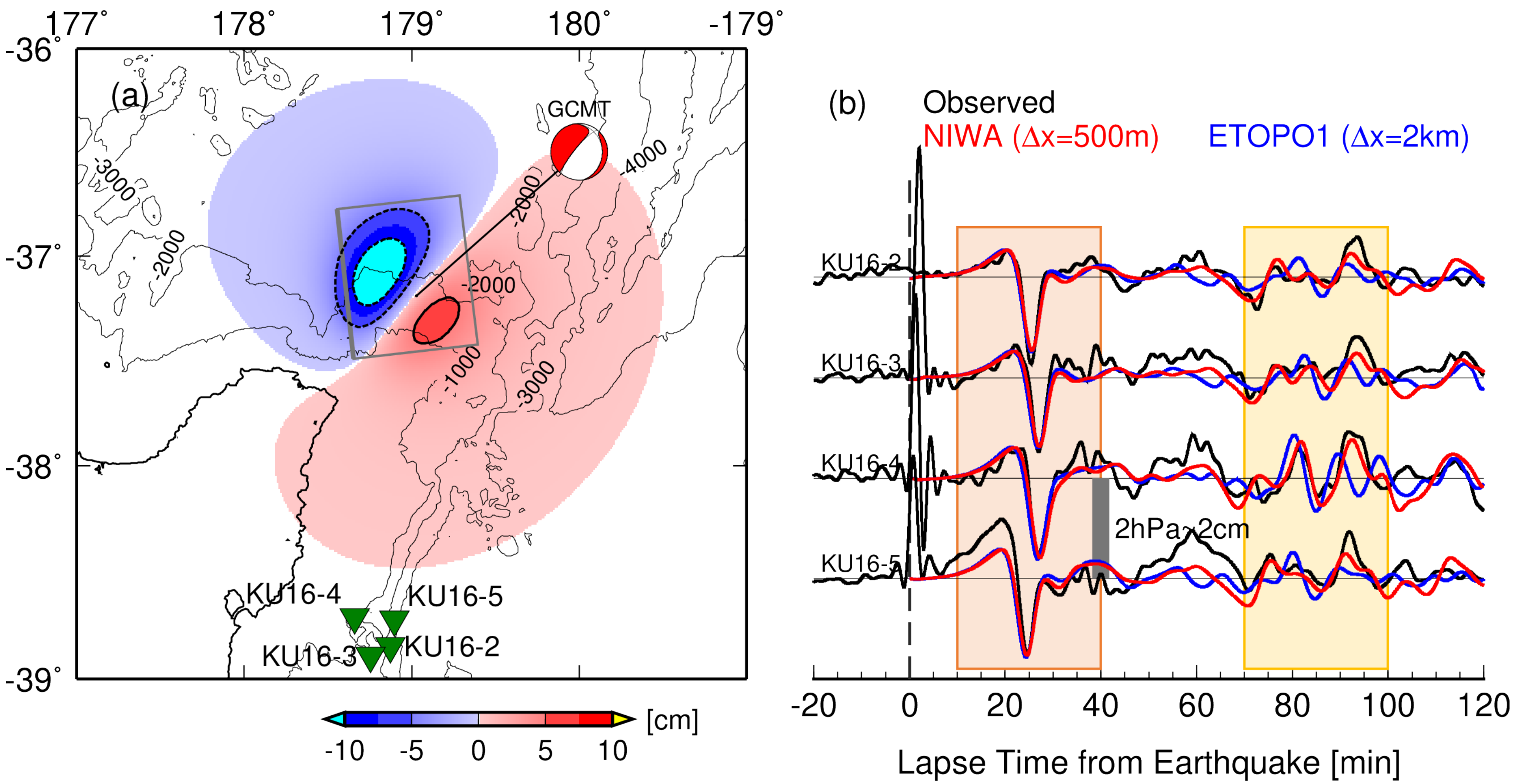

Figure S17. Comparison of the observed (black) and calculated waveforms based on the result of the finite fault inversion (Figure 8), with the NIWA bathymetry data (red) and ETOPO1 bathymetry data (blue).

Table S1. Time delay of tsunami arrival (τ_{ij}^{obs}) for the direct waves

Station *i*	Station *j*	Time delay from cross correlation [min][a]	Time delay from peak timing [min][b]
KU16-5	KU16-2	0.72	0.75
KU16-5	KU16-3	2.28	2.35
KU16-5	KU16-4	2.30	2.13
KU16-2	KU16-3	1.60	1.60
KU16-2	KU16-4	1.60	1.38
KU16-3	KU16-4	0.15	−0.22

[a]Time delay is measured by cross correlation (CC_{ij}). Positive time delay denotes that tsunami arrives earlier at station *i*.
[b] Time delay is measured by peak timing of tsunami, shown in Table 2. Positive time delay denotes that tsunami arrives earlier at station *i*.

Table S2. Time delay of tsunami arrival (τ_{ij}^{obs}) for the reflected waves

Station *i*	Station *j*	Time delay from cross correlation [min][a]	Time delay from peak timing [min][b]
KU16-5	KU16-4	0.78	−0.15
KU16-5	KU16-2	1.18	1.67
KU16-5	KU16-3	1.88	1.65
KU16-4	KU16-2	0.07	−1.82
KU16-4	KU16-3	1.25	1.80
KU16-2	KU16-3	0.65	1.60

[a]Time delay is measured by cross correlation (CC_{ij}). Positive time delay denotes that tsunami arrives earlier at station *i*.
[b] Time delay is measured by peak timing of tsunami, shown in Table 2. Positive time delay denotes that tsunami arrives earlier at station *i*.